OPTICS

NIR-switched DNA tweezer enables reversible miRNA recognition with erasable signal for in vivo continuous imaging

Caixia Wang[1]†, Yulin Cong[1]†, Linlin Yang[2]†, Liang Liu[1], Yuxin Xie[1], Xuan Ding[1], Guixiang Zeng[2]*, Huangxian Ju[1], Ying Liu[1,3]*

Continuous monitoring of miRNA expression in vivo is crucial for understanding complex biological processes. However, current miRNA imaging probes suffer from irreversible responses, impairing their capabilities for real-time tracking concentration fluctuations. Here, we present a near-infrared regulated DNA tweezer (NIR-DNA tweezer) with reversible binding affinities to target miRNA. Self-quenched DNA tweezer is composed of BHQ3-labeled miRNA recognition strand and Cy5-labeled competitive strand, while competitive strand is embedded with azobenzene (Azo) to photo-switch the hybridization zones of DNA tweezer for reversible miRNA recognitions. NIR-DNA tweezer is obtained by conjugating DNA tweezer to upconversion nanoparticles, which is switched to "transit" status upon high-power 808-nm irradiation with *cis*-Azo to allow miRNA recognition with Cy5 fluorescence recovery. Upon low-power 808-nm irradiation, NIR-DNA tweezer is switched to "closed" status with *trans*-Azo to release miRNA and erase signal. The as-presented NIR-DNA tweezer achieves real-time in vivo tracing of miRNA expression fluctuations upon continuous chemotherapeutic drug and inhibitor treatments.

INTRODUCTION

The concentrations and distributions of microRNAs (miRNAs) are closely associated with numerous of biological processes (*1*), including disease generation, progression, recovery, and body response to antitumor drugs (*2*, *3*). MiRNAs exhibit dynamic expression patterns in short periods of time corresponding to physiological condition changes. For example, miR-1264/1298/448 expression were up-regulated in cerebral ischemia process and demonstrated rapid increase in the first 150 min of reperfusion process, followed by decrease in 24 hours (*4*); MiR-30d-5p/miR-125b-5p was reported substantially enhanced in the initial phase of myocardial infarction (0 to 6 hours) with subsequent declining values in 24 hours (*5*). Therefore, continuous tracking its concentration fluctuation in real time is essential to investigate disease development and treatment processes and promote therapy (*6*, *7*).

While substantial advancements have been made for miRNA imaging via developing responsive nucleic acids structures and hybridization strategies (*8*–*12*), current reported miRNA probes are limited by their irreversible response modes, which makes it difficult to erase signal once it generates. Specifically, the imaging signal increases with miRNA expression rises but fails to decrease in real time upon miRNA concentration drops. The "one time" irreversible detection mode makes it challenging for in situ continuous tracking miRNA expression fluctuations. Although the in vivo signal would eventually decrease upon probe metabolization, it is an uncontrolled process and usually far lags behind the natural drop of miRNA expression.

Designing recognition probes with reversible binding affinities to target is the key for continuous tracking its concentration fluctuations. Given the high configurability of DNA through Watson-Crick base pairing (*13*), DNA self-assembled structures are well-suited for this purpose. The introduction of an inducer strand that competes with recognition strand for target molecule could release target and renew recognition strand (*14*). However, repetitive extra additions of inducer strand are required for multiple times measurements, which are labor-consuming and impair in vivo applications. Light-based manipulation offers high spatiotemporal control via a noninvasive mode (*15*), making it an attractive and effective approach for DNA configuration manipulation (*16*). Azobenzene (Azo) and similar photo-switcher molecules, which undergo photoisomerization under alternate different wavelength light exposures (*17*–*20*), have been incorporated with DNA strands for configuration controls (*21*–*23*) and biofunction manipulations (*20*). By connecting recognition strand and competitive strand with an Azo decorated linker strand, photo-reversible DNA probes have been successfully developed for adenosine 5′-triphosphate and thrombin detections (*24*–*26*). To guarantee the switching efficiency of Azo decorated linker strand, the hybridization zone between recognition strand and competitive strand are usually control below ~10 base pairs (bp), which limits their applications to small-molecule targets with weak binding affinities to recognition probes (*27*, *28*). In addition, the photo manipulation relies on ultraviolet (UV)–visible (Vis) light with shallow tissue penetration and phototoxicity (*29*), which further impede its in vivo application.

Here, we extend the detection target of photo-reversible probe from small molecules to nucleic acid. Take miRNA-21 (miR-21), whose expression fluctuation is associated with tumor progression and reflects different drugs effects (*30*, *31*) for example, its binding affinity to recognition probe has to be modulated in a much wider range to achieve reversible detection considering its around 21 bp of recognition zone. Therefore, it is required to directly modulate the hybridization zone of recognition/competitive strand instead of modulating linker strand configuration for reversible miR-21 detection. MiR-21 recognition probe (R-DNA) is consist of recognition region and linker region, while competitive probe ($C\text{-}DNA_{Azo}$) is consist of competitive region

[1]State Key Laboratory of Analytical Chemistry for Life Science, School of Chemistry and Chemical Engineering, Nanjing University, Nanjing 210023, China. [2]Kuang Yaming Honors School, Nanjing University, Nanjing 210023, China. [3]Chemistry and Biomedicine Innovation Center, Nanjing University, Nanjing 210023, China.
*Corresponding author. Email: yingliu@nju.edu.cn (Y.L.); gxzeng@nju.edu.cn (G.Z.)
†These authors contributed equally to this work.

and linker region. Competitive region in C-DNA$_{Azo}$ contains switchable region and clip region, and Azo molecules were incorporated in switchable region (Fig. 1A, R-DNA and C-DNA$_{Azo}$). DNA tweezer is obtained upon mixture of R-DNA and C-DNA$_{Azo}$, and its hybridization zones are directly switched upon alternative UV/Vis irradiations to achieve reversible miRNA detection. R-DNA and C-DNA$_{Azo}$ are fully hybridized with *Trans*-isomerization of Azo to keep DNA tweezer in "closed" status with low binding affinity to miR-21 (Fig. 1A, closed status). UV irradiation switches Azo to cis-isomerization, which dehybridizes C-DNA$_{Azo}$ and R-DNA in switchable region and converts DNA tweezer to "transit" status with partial exposure of miR-21 recognition region in R-DNA (Fig. 1A, transit status). The Transit DNA tweezer with spaced hybridized C-DNA$_{Azo}$ and R-DNA has much higher binding affinity to miR-21. The partial exposed miR-21 recognition region in R-DNA acts as toehold for miR-21 binding to DNA tweezer, which continuously dehybridizes C-DNA$_{Azo}$ and R-DNA in clip region and turns DNA tweezer to "open" status (Fig. 1A, open status). Vis irradiation turns Azo to trans-isomerization and rehybridizes R-DNA and C-DNA$_{Azo}$ in switchable region. With the linker region and switchable region acted as "hybridized toehold," C-DNA$_{Azo}$ is rehybridized to R-DNA, which releases miR-21 from DNA tweezer and renews it to closed status for reversible miR-21 detection (Fig. 1A, Vis).

To facilitate in vivo application, the as-obtained photo-switchable DNA tweezer is conjugated to upconversion nanoparticles (UCNPs) that convert near-infrared (NIR) irradiation with higher tissue penetration depth (*32*) to UV/Vis emissions. Multilayer-structured UCNP $NaYF_4$:Tm,Yb@$NaYF_4$,Yb,Nd@$NaYF_4$:Nd is synthesized, which produces high UV/Vis upconversion emission ratio upon high-power 808-nm irradiation and high Vis/UV upconversion emission ratio upon low-power 808-nm irradiation, respectively (Fig. 1B, UCNPs). After wrapping with DSPE-methoxy polyethylene glycol (DSPE-mPEG), DSPE–polyethylene glycol (PEG)– dibenzocyclooctyne (DBCO) and DSPE–PEG–folic acid (FA) for water dispersion and cancer cell targeting, the as-obtained UCNPs-DBCO/FA is then clicked with azide-functionalized DNA tweezer (N_3-DNA tweezer) to obtain NIR power density-regulated DNA tweezer (NIR-DNA tweezer) (Fig. 1B, NIR-DNA tweezer). For continuous in vivo miR-21 imaging, C-DNA$_{Azo}$ and R-DNA are labeled with fluorescent dye Cy5 and its corresponding quencher BHQ3, respectively, to make a self-quenched DNA tweezer in its closed status (Fig. 1C, NIR-DNA tweezer$_{Cy5/BHQ3}$, closed status). The as-obtained NIR-DNA tweezer$_{Cy5/BHQ3}$ is intravenously administrated to mice and selectively accumulated in folate receptor (FA)–expressed tumor cells. High-power 808-nm excitation induces cis-isomerization of Azo and results in "spaced hybridization" of C-DNA$_{Azo/Cy5}$ and R-DNA$_{BHQ3}$ for DNA tweezer with high binding affinity to miR-21. MiR-21 binding switches NIR-DNA tweezer$_{Cy5/BHQ3}$ to open status and recovers Cy5 fluorescence for miRNA imaging (Fig. 1C; 808 nm, high power). Considering the dynamic nature of miRNA expression in various physiological and pathological processes, resetting NIR-DNA tweezer to the closed status with signal erasing is crucial for continuous in vivo tracking of miRNA. Low-power 808-nm excitation, which induces trans-isomerization of Azo, reverses the binding activity of DNA tweezer to miRNA and closes NIR-DNA tweezer$_{Cy5/BHQ3}$ with Cy5 fluorescence quenched and miRNA release (Fig. 1C; 808 nm, low power). By alternatively irradiating tumor grown position with high-power and low-power 808-nm light, NIR-DNA tweezer$_{Cy5/BHQ3}$ is reversibly switched between open and closed status, which allows controllable capture and release of miR-21 for continuous imaging of its in vivo expression fluctuations. This approach offers potential for dynamic in vivo monitoring of various nucleic acid markers and would contribute to disease progression and recovery evaluations.

RESULTS

Synthesis of DNA tweezer with photo-regulated azo isomerization conversions

MiR-21 recognition probe (R-DNA) and competitive probe (C-DNA$_{Azo}$) were prepared by extending both miR-21 recognition region and competitive region with a 12-bp linker region. Four Azo molecules are incorporated at alternating bases within the 8-bp C-DNA's switchable region that locates between linker region and 14-bp clip region. R-DNA and C-DNA$_{Azo}$ have complimentary sequence except 2-bp mismatch in clip region to facilitate miR-21 recognition (Fig. 1A, R-DNA and C-DNA$_{Azo}$). DNA tweezer was synthesized by hybridization of R-DNA and C-DNA$_{Azo}$, competitive region in C-DNA$_{Azo}$ was responsive for reversible modulation of miR-21 binding affinity, while linker region guaranteed structure stability during DNA tweezer status switching process. The synthesis of DNA tweezer was confirmed by polyacrylamide gel electrophoresis (PAGE) analysis, which showed a new band with lower mobility (fig. S1, lane 3) upon mixture of R-DNA (fig. S1, lane 1) and C-DNA$_{Azo}$ (fig. S1, lane 2). UV/Vis spectroscopy confirmed the reversible photoisomerization of Azo. UV irradiation induced decrease of $\pi \rightarrow \pi^*$ absorption peak at 330 nm (*33*, *34*) and increase of $n \rightarrow \pi^*$ absorption peak at 440 nm (*33*, *34*) (fig. S2A; UV), confirming the trans-to-cis isomerization conversion of Azo. Subsequent Vis irradiation resulted in increase of absorption peak at 330 nm and decrease of absorption peak at 440 nm, confirming the reverse cis-to-trans isomerization conversion of Azo (fig. S2A; Vis after UV). Accordingly, C-DNA$_{Azo}$ demonstrated similar intensity change tendency for 330-nm characteristic absorption peak corresponding to alternate UV and Vis irradiation, while DNA characteristic absorption peak at 260 nm remained unchanged (fig. S2B), indicating the efficient isomerization switch of Azo in C-DNA$_{Azo}$.

Photo-switchable response of DNA tweezer to miRNA

To verify its reversible binding to MiR-21, fluorescent dye 5-Carboxyfluorescein (FAM) and its corresponding quencher Black Hole Quencher-1 (BHQ1) were labeled on C-DNA$_{Azo}$ and R-DNA, respectively, to prepare self-quenched DNA tweezer$_{FAM/BHQ1}$ in its closed status [Fig. 2A, before irradiation (BI)]. UV light irradiation caused Azo's trans-to-cis isomerization, thereby disrupted hydrogen bonds between DNA double strands in switchable region and resulted in "spaced hybridized" R-DNA$_{BHQ1}$ and C-DNA$_{Azo/FAM}$ with high binding affinity to miR-21. Corresponding miR-21 recognition turned DNA tweezer$_{FAM/BHQ1}$ to open status with FAM fluorescence recovery (Fig. 2A, first UV). In the absence of miR-21, the clip region in DNA tweezer$_{FAM/BHQ1}$ remained hybridized in transit status and barely showed FAM fluorescence [fig. S3, UV(+), miR-21(−)]. In the absence of UV irradiation to generate unhybridized loop in switchable region, miR-21 failed to hybridize to DNA tweezer$_{FAM/BHQ1}$ and could not show FAM fluorescence recovery [fig. S3, UV(−), miR-21(+)]. These results indicated efficient light manipulation of DNA tweezer recognition capability to target miR-21.

Subsequent Vis irradiation switched DNA tweezer$_{FAM/BHQ1}$ to closed status with release of miR-21 and FAM fluorescence quench (Fig. 2A, first Vis). By alternately exposing DNA tweezer$_{FAM/BHQ1}$ under UV and Vis irradiations, it was switched between open and closed

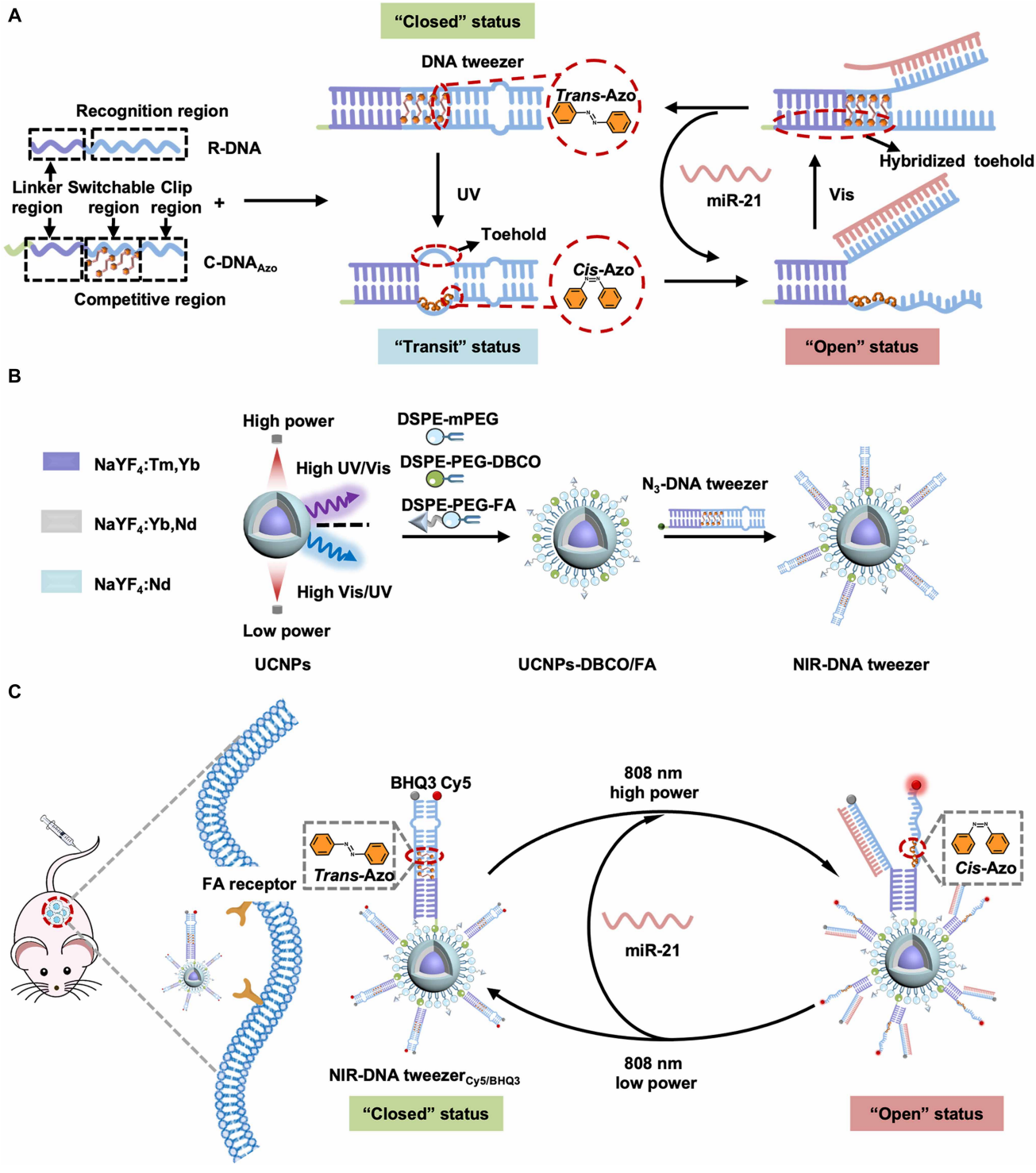

Fig. 1. Schematic illustrations of NIR-DNA tweezer for continuous in vivo miRNA imaging. (**A**) DNA tweezer construction and its status conversions upon alternate UV/Vis exposure and miR-21, (**B**) construction of NIR-DNA tweezer, and (**C**) its application for continuous in vivo miR-21 imaging.

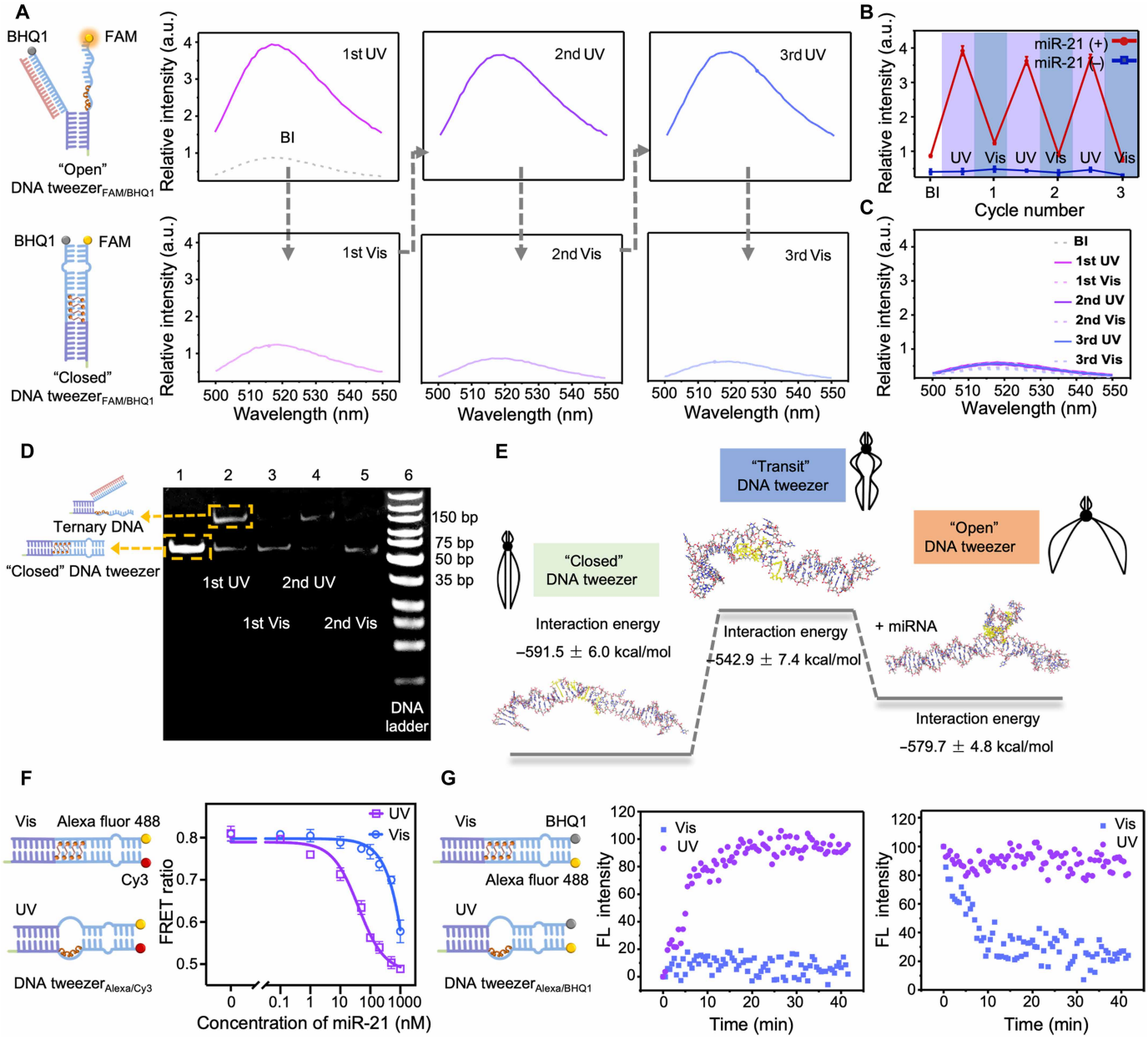

Fig. 2. Characterization of photo-switchable NIR-DNA tweezer for in vitro reversible miRNA detection. Fluorescence (FL) spectra of DNA tweezer$_{FAM/BHQ1}$ BI and in response to alternate UV/Vis irradiations (**A**) in the presence and (**C**) absence of miR-21 and (**B**) corresponding relative FAM fluorescence intensity. (**D**) PAGE assay of DNA tweezer for reversible capture and release of miR-21: lane 1: DNA tweezer; lane 2 and lane 4: DNA tweezer with target miR-21 after UV irradiation; lane 3 and lane 5: lane 2 and 4 after Vis irradiation; lane 6: DNA ladder. (**E**) Schematic illustrations of MD simulation (400 ns) and corresponding interaction energy for open, transit, and closed DNA tweezer. (**F**) FRET-based binding curves of DNA tweezer$_{Alex/Cy3}$ to miR-21 and (**G**) fluorescence kinetics analysis of miR-21 binding to and release from DNA tweezer$_{Alex/BHQ1}$ upon UV and Vis exposures, respectively. Error bars indicated means ± SD (n = 3). a.u., arbitrary unit.

statuses with reversible miR-21 binding and release. The "UV/Vis" alternate irradiation cycles were repeated three times, and the intensity of recovered FAM fluorescence maintained at similar levels {Fig. 2, A (second UV and third UV) and B [UV, miR-21 (+)]}. The good switching reversibility ensured the feasibility of photo-switchable DNA tweezer for continuous miRNA imaging. In the absence of miR-21, FAM fluorescence remained quenched during UV/Vis alternate exposure cycles {Fig. 2, B [miR-21 (–)] and C}. PAGE analysis also confirmed the photo-reversible binding of miR-21 to DNA tweezer. Open status DNA tweezer with miR-21 binding resulted in a ternary structure and exhibited lower mobility compared with closed DNA tweezer. Therefore, alternate UV/Vis irradiations demonstrated repetitive deepened/lightened patterns for ternary DNA band and lightened/deepened patterns for closed DNA tweezer band (Fig. 2D).

Molecular dynamics (MD) simulations were further performed to explore the dynamic structural changes of DNA under UV/Vis

light irradiation and during miR-21 hybridization/dehybridization. For model construction, Azo was conjugated to the nucleic acid backbone using a D-threoninol linker (fig. S4). Two DNA tweezer configurations were established: a closed DNA tweezer with Azo molecules in the trans-isomer form (fig. S5A) and a transit DNA tweezer with Azo in the *cis*-isomer form (fig. S6A). Both systems were simulated for 400 ns. The closed DNA tweezer maintained a stable double-helical structure throughout the simulation (fig. S5B). In contrast, the transit DNA tweezer exhibited a loss of double-helical integrity near the *cis*-Azo site (fig. S6B), suggesting that the trans-to-cis isomerization of Azo destabilizes the DNA duplex structure. Subsequently, an open DNA tweezer was constructed by hybridizing miR-21 to the transit DNA tweezer (fig. S7A). Over the 400-ns simulation, R-DNA maintained a stable double helix with miR-21 and a segment of C-DNA_{Azo}, while the remaining bases of C-DNA_{Azo} self-folded (fig. S7B).

To compare structural stability, the average interaction energies of the closed, transit, and open DNA tweezers were calculated using 5001 configurations sampled from the 350- to 400-ns MD trajectories. The interaction energies were -591.5 ± 6.0 kcal/mol for the closed state, -542.9 ± 7.4 kcal/mol for the transit state, and -579.7 ± 4.8 kcal/mol for the open state (Fig. 2E, table S1, and fig. S8). UV irradiation provided energy to the closed DNA tweezer, triggering trans-to-cis isomerization of Azo, which weakened interstrand interactions and resulted in the less stable "transit" state with higher interaction energy. Subsequent miR-21 binding restabilized the structure into the open state, reducing its overall energy (Fig. 2E).

The photo manipulation of reversible miR-21 binding affinities for DNA tweezer was evaluated through a fluorescence resonance energy transfer (FRET)–based binding assay. DNA $tweezer_{Alex/Cy3}$ was prepared with Alexa Fluor 488–labeled R-DNA_{Alex} and C-$DNA_{Azo/Cy3}$. Binding of miR-21 to DNA $tweezer_{Alex/Cy3}$ caused the separation of R-DNA_{Alex} and C-$DNA_{Azo/Cy3}$ with decrease of FRET signal. UV irradiation induced transit status of DNA $tweezer_{Alex/Cy3}$, partially exposed miR-21 recognition region, and endowed it high binding affinity to miR-21 with K_d (dissociation constant) value of ~21.74 nM, while Vis irradiation induced closed status of DNA $tweezer_{Alex/Cy3}$ and decreased miR-21 binding affinity to ~1880 nM (Fig. 2F). The photo-switched hybridization zones exhibited more than 80-fold difference of miR-21 binding affinities, which was much larger compared with the binding affinities conversion ranges of photo-switched linker strands that previously reported (*24*). The time corresponding fluorescence recovery for DNA tweezer in two status was also evaluated with DNA $tweezer_{Alex/BHQ1}$ that composed of R-DNA_{BHQ1} and C-$DNA_{Azo/Alex}$. Upon UV irradiation, transit status DNA $tweezer_{Alex/BHQ1}$ in the presence of 100 nM miR-21 exhibited substantial Alexa fluorescence recovery with fluorescence saturated at ~20 min, whereas closed status DNA $tweezer_{Alex/BHQ1}$ upon Vis irradiation barely showed Alex fluorescence recovery (Fig. 2G, binding). Subsequent Vis irradiation induced efficient release of miR-21 from open DNA $tweezers_{Alex/BHQ1}$ and quenched Alexa fluorescence to baseline level within 20 min (Fig. 2G, release).

Power density switched NIR-DNA tweezer for reversible miRNA detection

UCNPs were synthesized according to previously reported procedure (*35*). The upconversion core $NaYF_4$:0.5% Tm, 30% Yb showed a uniform size of 22.35 ± 0.48 nm (fig. S9, A and C) and barely generated UV/Vis upconversion emission under 808-nm excitation (fig. S10). Inner shell $NaYF_4$:10% Yb, 40% Nd grown increased particle size to 28.09 ± 1.0 nm (fig. S9, B and D), and outer shell $NaYF_4$:40% Nd grown increased particle size to 35.6 ± 1.2 nm (Fig. 3A and fig. S9E) with strong upconversion emission at UV (345/360 nm) and Vis (450/475 nm) regions under 808-nm excitation (fig. S10, UCNPs) due to the sensitization of Nd^{3+}-doped outer shells. The intensity ratio of UCNPs upconversion emission at Vis and UV regions (I_{Vis}/I_{UV}) was modulated through adjusting power of 808-nm excitation laser (*36*, *37*), which decreased with laser power (fig. S11). Visible emission dominated the upconversion emission spectrum with I_{Vis}/I_{UV} of 3.06 at low excitation power of 0.028 W (Fig. 3B, low power), while UV emission was intense at high excitation power, and I_{Vis}/I_{UV} was saturated at 1.39 with excitation power of 1.16 W (Fig. 3B, high power).

The $\pi \rightarrow \pi^*$ characteristic absorption band of *trans*-Azo at 330 nm and $n \rightarrow \pi^*$ characteristic absorption band of *cis*-Azo at 440 nm overlapped with UV upconversion emission peaks and Vis upconversion emission peaks of UCNPs, respectively (fig. S12). The molar attenuation coefficient of Azo trans-isomer (22,000 M^{-1} cm^{-1}) (*38*) is much larger than that of Azo cis-isomer (400 M^{-1} cm^{-1}) (*38*). Therefore, when UV upconversion emission in 345-/360-nm region is strong enough upon high-power 808-nm excitation, its emission energy is used more efficiently compared with that of Vis upconversion emission in 450-/475-nm region, which facilitates trans-to-cis isomerization of Azo. On the other hand, the UV upconversion emission of UCNPs is too weak to make an effect at low-power 808-nm excitation; thus, the dominant Vis upconversion emission region in 450/475 nm takes effort to drive the reverse cis-to-trans isomerization of Azo. To confirm Azo isomer conversion via manipulating NIR irradiation powers, its absorbance was kept measured upon 90-min, high power density 808-nm laser exposure (2 W/cm^2), which demonstrated gradual decrease of $\pi \rightarrow \pi^*$ characteristic absorption band for *trans*-Azo at 330 nm with gradual increase of $n \rightarrow \pi^*$ characteristic absorption band for *cis*-Azo at 440 nm, confirming the trans-to-cis photoisomerization of Azo (fig. S13A). On the contrary, *trans*-Azo characteristic absorption band at 330 nm gradually increased with 90-min, low power density 808-nm exposure (0.75 W/cm^2), in accordance with the gradual decrease of *cis*-Azo characteristic absorption band at 440 nm (fig. S13B). These results confirmed the feasibility of modulating Azo isomerization via regulating NIR irradiation power density.

UCNPs were wrapped with amphiphilic polymer DSPE-PEG, DSPE-PEG-DBCO, and DSPE-PEG-FA via hydrophobic-hydrophobic interaction to obtain UCNPs-DBCO/FA with zeta potential of -1.87 ± 0.45 mV and hydrodynamic size of 59 ± 2.9 nm (Fig. 3C, UCNPs-DBCO/FA). NIR-DNA tweezer was prepared by conjugating N_3-DNA tweezer to UCNPs-DBCO/FA, which showed reduced UCNP upconversion emissions at 345/360 nm due to the absorption of Azo in DNA strands (fig. S14), confirming the successful conjugation of DNA tweezer to UCNPs and demonstrating more negative zeta potential of -17.3 ± 0.17 mV and larger hydrodynamic size of 81 ± 1.5 nm (Fig. 3C, NIR-DNA tweezer). To further quantify the amount of DNA tweezer on UCNPs surface, N_3-DNA $tweezer_{FAM}$ was conjugated to UCNPs-DBCO/FA to obtain NIR-DNA $tweezer_{FAM}$, which demonstrated FAM characteristic peak at 520 nm under 480-nm excitation (fig. S15A). The corresponding FAM fluorescence intensity was quantified (fig. S15, B and C) to obtain surface DNA tweezer coverage of 132 ± 15 per particle. The kinetic reactions of NIR-DNA $tweezer_{Alex/BHQ1}$ with miR-21 were studied under high-/low- power

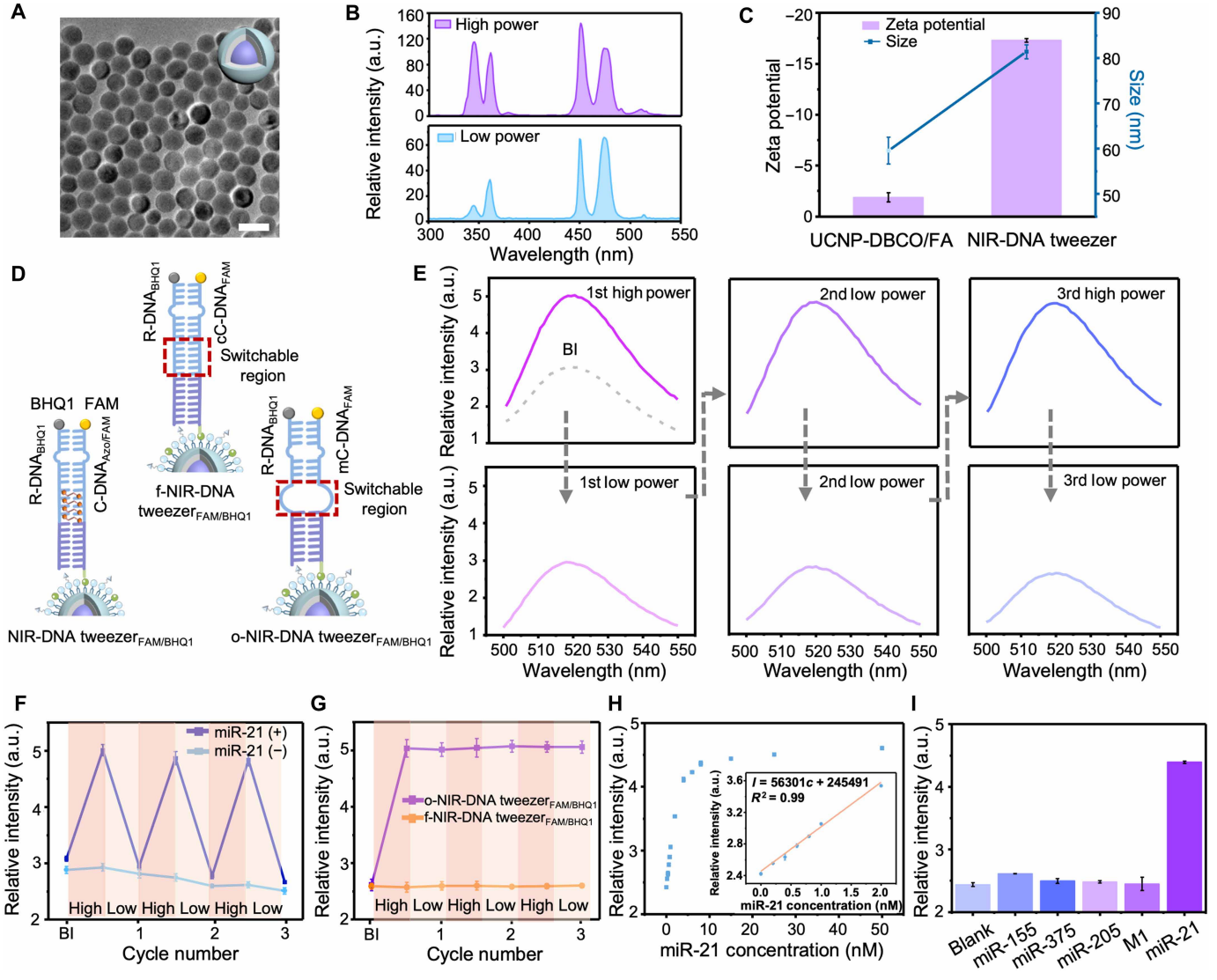

Fig. 3. Power density switched NIR-DNA tweezer for in vitro reversible miRNA detection. (**A**) Transmission electron microscopic images of UCNP $NaYF_4$:Tm,Yb@$NaYF_4$:Yb,Nd@$NaYF_4$:Nd. Scale bar, 50 nm. (**B**) Upconversion emission spectra of UCNPs in cyclohexane under 808-nm laser irradiation with high-power and low-power 808-nm NIR excitations. (**C**) Zeta potential and hydrodynamic size of UCNPs-DBCO/FA and NIR-DNA tweezer. (**D**) Schematic illustrations of NIR-DNA tweezer$_{FAM/BHQ1}$, f-NIR-DNA tweezer$_{FAM/BHQ1}$, and o-NIR-DNA tweezer$_{FAM/BHQ1}$. (**E**) Fluorescence spectra of DNA tweezer FAM/BHQ1 in the presence of miR-21 BI and after three cycle of alternate high power density and low power density 808-nm NIR irradiation. Relative FAM fluorescence intensity of (**F**) NIR-DNA tweezer$_{FAM/BHQ1}$ in the presence and absence of miR-21 and (**G**) f-NIR-DNA tweezer$_{FAM/BHQ1}$ and o-NIR-DNA tweezer$_{FAM/BHQ1}$ in the presence of miR-21 after three cycle of alternate high power density and low power density 808-nm NIR irradiation. Relative FAM fluorescence intensity of (**H**) NIR-DNA tweezer$_{FAM/BHQ1}$ in response to 0.2 to 50 nM miR-21 under high-power 808-nm irradiations. Inset shows the calibration curve for miR-21 and (**I**) miR-21 and nonspecific miRNAs under high-power 808-nm irradiations. Error bars indicated means ± SD (n = 3).

808-nm NIR irradiations. Upon high-power 808-nm irradiation, NIR-DNA tweezers effectively bound miR-21 with Alexa fluorescence recovery saturated in approximately 30 min (fig. S16A). Subsequent low-power 808-nm irradiation facilitated efficient release of miR-21 with Alexa fluorescence quenched to baseline levels within 30 min (fig. S16B).

To trace the status switching of NIR-DNA tweezer with reversible miR-21 binding and release, N_3-DNA tweezer$_{FAM/BHQ1}$ was conjugated to UCNPs-DBCO/FA via click reaction to obtain NIR-DNA tweezer$_{FAM/BHQ1}$ (Fig. 3D, NIR-DNA tweezer$_{FAM/BHQ1}$). Alternate 808-nm NIR irradiations with high and low power densities switched Azo trans- and cis-isomers, which modulated hybridization zones in DNA tweezer, and converted its status among closed and open with the participation of miR-21. High power density 808-nm laser irradiation converted Azo from trans-isomer to cis-isomer, which hybridized miR-21 with recognition region and turned DNA tweezer$_{FAM/BHQ1}$ to open status and recovered FAM fluorescence (Fig. 3E, first high power). Low power density 808-nm laser radiation was subsequently applied, which reversed Azo from cis-isomer to trans-isomer and thus reversed NIR-DNA tweezer$_{FAM/BHQ1}$ to closed status with release of miR-21 and FAM fluorescence quench (Fig. 3E, first low power). The switching of high power density and low power density 808-nm irradiations were repeated for three cycles and demonstrated regular FAM fluorescence recovery upon high power density 808-nm

laser irradiation (Fig. 3E, second and third high power) and FAM fluorescence quench upon low power density 808-nm laser irradiation (Fig. 3E, second and third low power) in three cycles [Fig. 3F, miR-21 (+)], indicating good NIR regulated reversible response of NIR-DNA tweezer$_{FAM/BHQ1}$ to miR-21. In the absence of miR-21, NIR-DNA tweezer$_{FAM/BHQ1}$ was failed to convert closed to open status and thus could not recover FAM fluorescence [Fig. 3F, miR-21(−), and fig. S17A]. As control groups, fastened NIR-DNA tweezer$_{FAM/BHQ1}$ (f-NIR-DNA tweezer$_{FAM/BHQ1}$) that features an azo-free switching region and always stayed in closed status (Fig. 3D, f-NIR-DNA tweezer$_{FAM/BHQ1}$) was synthesized and incubated with miR-21 with alternative high/low power density 808-nm NIR irradiations, which demonstrated little FAM fluorescence change due to the complete seal of miR-21 recognition region [Fig. 3G (f-NIR-DNA tweezer$_{FAM/BHQ1}$) and fig. S17B]. In addition, opened NIR-DNA tweezer$_{FAM/BHQ1}$ (o-NIR-DNA tweezer$_{FAM/BHQ1}$) that has mismatched 8 bp in switchable region instead of Azo modification and always stayed in open status (Fig. 3D, o-NIR-DNA tweezer$_{FAM/BHQ1}$) was synthesized and incubated with miR-21 with alternative high/low power density 808-nm NIR irradiations, which all showed strong FAM fluorescence [Fig. 3G (o-NIR-DNA tweezer$_{FAM/BHQ1}$) and fig. S17C]. These results confirmed the importance of photo-switchable hybridization zones in NIR-DNA tweezer for reversible miRNA detection.

The biosensing capability of NIR-DNA tweezer$_{FAM/BHQ1}$ was evaluated by incubating with various concentrations of miR-21, demonstrating a linear range of 0.2 to 2.0 nM and a limit of detection of 92.3 pM (Fig. 3H and fig. S18A), which was comparable to previously reported miRNA detection probes (*7*). Detection specificity was also evaluated by incubating NIR-DNA tweezer$_{FAM/BHQ1}$ with 50 nM miR-155, miR-205, miR-375, and single-base mismatched miRNA-21 (M1), which all showed negligible fluorescence recovery after high power density 808-nm laser irradiation (Fig. 3I and fig. S18B), indicating good detection specificity of NIR-DNA tweezer.

NIR-DNA tweezer for intracellular dynamic miRNA imaging

The Cell Counting Kit-8 (CCK-8) assay was performed to investigate the cytotoxicity of NIR-DNA tweezer and NIR irradiation power switching. NIR-DNA tweezer (up to 200 μg/ml) and high- (2 W/cm^2)/low power density (0.75 W/cm^2) of 808-nm laser irradiation all showed above 93% cell viability (fig. S19).

NIR-DNA tweezer$_{Red}$ was synthesized by conjugating N_3-DNA tweezer$_{Red}$ to UCNPs-DBCO/FA to trace the internalization and endosomal escape of NIR-DNA tweezer. DNA tweezer$_{red}$ was synthesized with R-DNA and Texas red–labeled C-DNA$_{Azo/red}$ (fig. S20A). Increased colocalization of Texas red fluorescence with LysoTracker fluorescence was observed during 6- to 9-hour incubation period with highest Pearson's correlation coefficient (PCC) of 0.87 reached at 9 hours, indicating efficient internalization of NIR-DNA tweezer$_{Red}$ (fig. S20, B and C, 6 to 9 hours). The gradual separation of Texas red and LysoTracker fluorescence was observed after 9 hours, with PCC decreased to 0.44 at 11 hours and 0.28 at 12 hours (fig. S20, B and C, 10 to 12 hours), indicating efficient transfer of NIR-DNA tweezer$_{Red}$ from endosome to cytoplasm. To verify probe structure integrity during experiment period, NIR-DNA tweezer$_{Red}$ was incubated with HeLa cells for 24 hours, which still showed good overlap of UCNP upconversion emission at 450 nm and Texas red fluorescence at 615 nm with PCC of 0.73 (fig. S21), indicating the intracellular structure integrity of NIR-DNA tweezer.

NIR-DNA tweezer$_{Cy3/BHQ2}$ was constructed and incubated with HeLa cells for continuous intracellular imaging. The as-obtained NIR-DNA tweezer$_{Cy3/BHQ2}$ stayed in closed status and showed little intracellular Cy3 fluorescence before light irradiation (Fig. 4A, BI). High power density of 808-nm laser radiation and the corresponding miR-21 binding switched NIR-DNA tweezer$_{Cy3/BHQ2}$ to open status and recovered intracellular Cy3 fluorescence (Fig. 4A, high, first cycle). The subsequent exposure of HeLa cells with low power density 808-nm radiation quenched intracellular Cy3 fluorescence (Fig. 4A, low, first cycle), suggesting that NIR-DNA tweezer$_{Cy3/BHQ2}$ was reversed to closed status with the release of miRNA-21. In the next cycle of alternate high power density/low power density 808-nm NIR irradiation, intracellular Cy3 fluorescence displayed similar intensity conversion trend of recovery and quench respectively (Fig. 4A, second cycle). Compared with intracellular Cy3 fluorescence recovery in response to first high-power 808-nm irradiation, second high-power 808-nm irradiation recovered 96.5% of intracellular Cy3 fluorescence (Fig. 4B, group 2, first high and second high), indicating good intracellular reversibility of NIR-DNA tweezer. As the "nonresponsed control," f-NIR-DNA tweezer$_{Cy3/BHQ2}$ was prepared with an azo-free switching region, which always remained in closed status and showed little intracellular Cy3 fluorescence recovery to both high- and low power density 808-nm irradiation [Fig. 4B (group 1) and fig. S22A]. As the "irreversible control," o-NIR-DNA tweezer$_{Cy3/BHQ2}$ was also prepared with mismatched 8 bp in switchable region instead of Azo modification, which remained in open status and showed intracellular Cy3 fluorescence regardless of 808-nm irradiation power switch [Fig. 4B (group 3) and fig. S22B]. Intracellular fluorescence kinetic studies of NIR-DNA tweezer$_{Cy3/BHQ2}$ interaction with miRNA-21 were also performed under high-power and low-power 808-nm NIR irradiations, respectively. High-power 808-nm NIR irradiation resulted in intracellular Cy3 fluorescence saturation within ~30 min (fig. S23, A and C), while subsequent low-power 808-nm irradiation suppressed signal to baseline level within ~30 min (fig. S23, B and D), confirming intracellular operational feasibility of NIR-DNA tweezer$_{Cy3/BHQ2}$.

To verify the feasibility of NIR-DNA tweezer$_{Cy3/BHQ2}$ for dynamically tracing intracellular miRNA expression fluctuation, NIR-DNA tweezer$_{Cy3/BHQ2}$–treated HeLa cells were first exposed with one cycle of alternate high-/low-power 808-nm NIR irradiation, which showed Cy3 fluorescence recovery and quench, respectively (Fig. 4C, group 1, BI, first cycle). The as-treated cells were then incubated with miR-21 mimic to up-regulate intracellular miR-21 expression, which demonstrated enhanced intracellular Cy3 fluorescence upon high-power 808-nm laser radiation (Fig. 4C, group 1, second cycle, high). The intracellular Cy3 fluorescence intensity was 1.86-fold compared with that of HeLa cells under high-power 808-nm laser radiation in first cycle (Fig. 4D, first cycle, high and second cycle, high). Obvious quenching of Cy3 fluorescence was observed under subsequent low-power 808-nm laser radiation, indicating efficient release of miR-21 and renewal of NIR-DNA tweezer$_{Cy3/BHQ2}$ back to closed status (Fig. 4C, group 1, second cycle, low). The as-treated cells were subsequently incubated with miR-21 inhibitor to mimic the down-regulation of intracellular miR-21 expression, and intracellular Cy3 fluorescence was correspondingly largely suppressed after high power density irradiation (Fig. 4C, group 1, third cycle, high). The intracellular Cy3 fluorescence intensity was about 16.61% compared with that of HeLa cells under high-power 808-nm laser radiation in the first cycle (Fig. 4D, first cycle, high and third cycle, high). Subsequent low-power 808-nm laser radiation reversed NIR-DNA tweezer$_{Cy3/BHQ2}$ to closed status and quenched Cy3 fluorescence back to original level (Fig. 4C, group

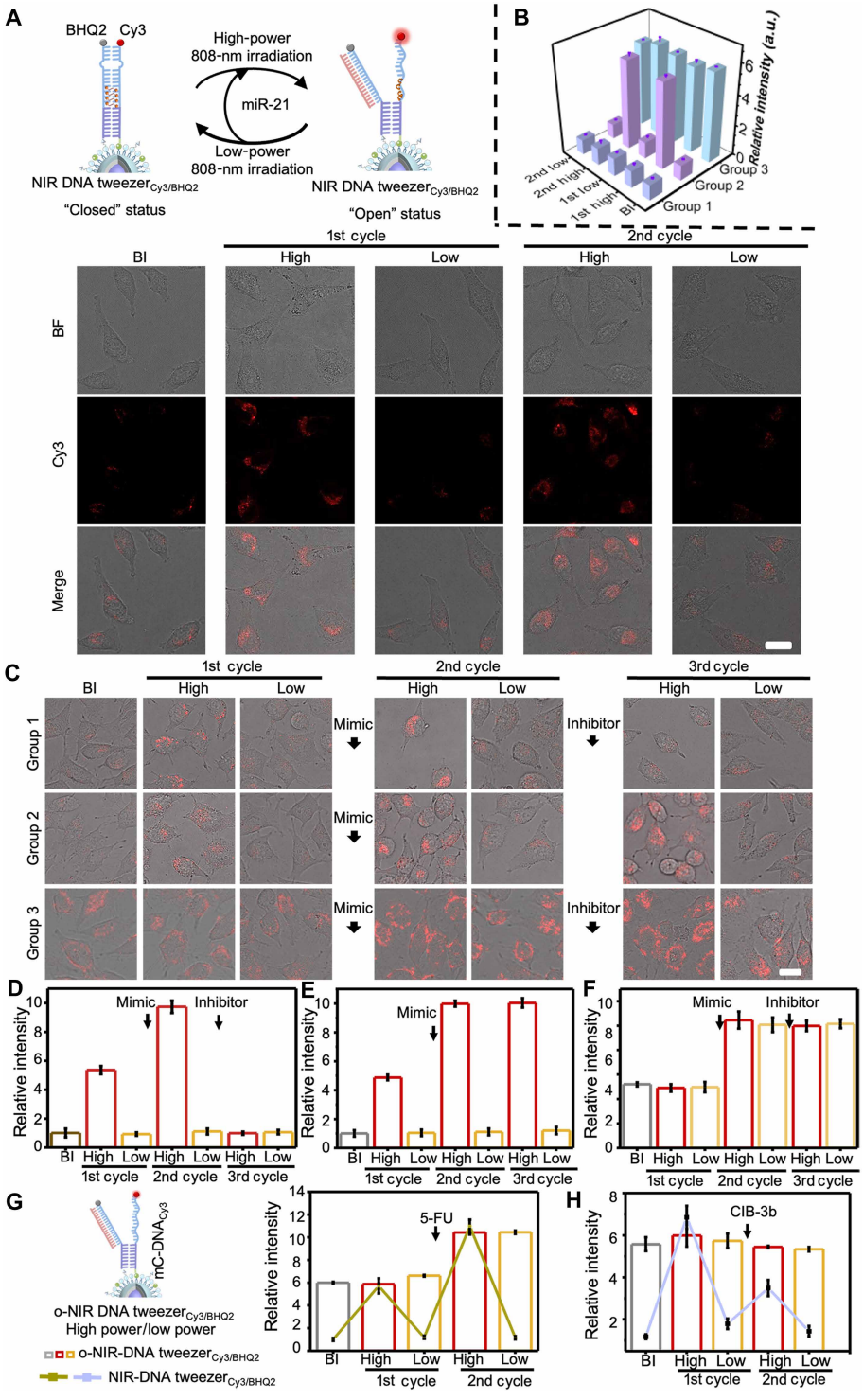

Fig. 4. NIR-DNA tweezer for intracellular dynamic miRNA imaging. (**A**) CLSM fluorescence imaging of HeLa cells incubated with NIR-DNA tweezer$_{Cy3/BHQ2}$ and (**B**) relative intracellular Cy3 fluorescence intensity in HeLa cells treated with group 1 f-NIR-DNA tweezer$_{Cy3/BHQ2}$, group 2 NIR-DNA tweezer$_{Cy3/BHQ2}$, and group 3 o-NIR-DNA tweezer$_{Cy3/BHQ2}$ under two cycles of alternate high (2 W/cm^2) and low (0.75 W/cm^2) power density 808-nm irradiation. (**C**) CLSM fluorescence imaging of HeLa cells incubated with group 1 NIR-DNA tweezer$_{Cy3/BHQ2}$ and subsequent treated with miR-21 mimic and inhibitor, group 2 NIR-DNA tweezer$_{Cy3/BHQ2}$ and subsequent treated with miR-21 mimic, and group 3 o-NIR-DNA tweezer$_{Cy3/BHQ2}$ and subsequent treated with miR-21 mimic and inhibitor under three cycles of alternate high (2 W/cm^2) and low (0.75 W/cm^2) power density 808-nm radiation (NIR-DNA tweezer$_{Cy3/BHQ2}$ was gently centrifuged, and the supernatant were collected for cellular internalization), and corresponding intracellular relative Cy3 fluorescence intensity for (**D**) group 1, (**E**) group 2, and (**F**) group 3. (**G**) Intracellular relative Cy3 fluorescence intensity of NIR-DNA tweezer$_{Cy3/BHQ3}$ and o-NIR DNA tweezer$_{Cy3/BHQ3}$, respectively, incubated HeLa cells treated with (G) 5-FU (10 μM) and (**H**) CIB-3b (10 μM) under two cycles of alternate high (2 W/cm^2) and low (0.75 W/cm^2) power density 808-nm radiation. Error bars indicated means ± SD (n = 5). Scale bar in (A) and (C), 20 μm.

1, third cycle, low). To confirm the Cy3 fluorescence suppression upon miR-21 inhibitor was due to miR-21 expression decrease instead of nonspecific intracellular fluorescence quench, NIR-DNA tweezer$_{Cy3/BHQ2}$–treated HeLa cells was treated with miR-21 mimic and repeatedly exposed to alternate high-power, low power density 808-nm laser irradiations for two times, which showed same intracellular Cy3 fluorescence intensities each time after high-power 808-nm laser irradiation [Fig. 4, C (group 2) and E (second cycle high and third cycle, high)], indicating good reversibility of NIR-DNA tweezer for intracellular miR-21 imaging. Intracellular miR-21 expression was also quantified via polymerase chain reaction (PCR) (fig. S24, A and B), which demonstrated similar tendency as intracellular Cy3 fluorescence recovery, about 1.58-fold for miR-21 mimic–treated HeLa cells and 13.90% for miR-21 mimic and miR-21 inhibitor consecutively treated HeLa cells compared with that of untreated HeLa cells (fig. S24, C and D). These results indicated the feasibility of NIR-DNA tweezer for monitoring dynamic intracellular miR-21 expression fluctuation. On the contrary, o-NIR-DNA tweezer$_{Cy3/BHQ2}$ demonstrated obvious intracellular Cy3 fluorescence once incubated with HeLa cells (Fig. 4C, group 3, BI), and the fluorescence remained unchanged upon high-/low-power 808-nm laser irradiations [Fig. 4, C (group 3, first cycle) and F (first cycle)]. HeLa cells were then successively incubated with miR-21 mimic and miR-21 inhibitor. Although it showed obvious Cy3 fluorescence enhancement after miR-21 mimic incubation [Fig. 4, C (group 3, second cycle) and F (second cycle)], o-NIR-DNA tweezer$_{Cy3/BHQ2}$ failed to trace miR-21 expression decrease after miR-21 inhibitor incubation due to the structure irreversibility and barely demonstrated decrease of intracellular Cy3 fluorescence [Fig. 4, C (group 3, third cycle) and F (third cycle)]. Considering that the intracellular fluorescence intensity could well return to background intensity each time after low-power 808-nm NIR irradiation, as long as "signal erasing" step of low-power NIR irradiation is performed between two high power NIR irradiations, changing signal acquiring order and irradiation power pattern did not affect signal intensity (fig. S25).

NIR-DNA tweezer$_{Cy3/BHQ2}$ was then applied for dynamically monitoring intracellular miRNA expression change corresponding to drug treatments. HeLa cells were incubated with NIR-DNA tweezer$_{Cy3/BHQ2}$ and irradiated with consecutive high-/low-power 808-nm irradiations, which demonstrated Cy3 fluorescence recovery and quench, respectively [Fig. 4G (NIR-DNA tweezer$_{Cy3/BHQ2}$, first cycle) and fig. S26 (first cycle)]. Subsequently, NIR-DNA tweezer$_{Cy3/BHQ2}$–incubated HeLa cells were treated with 5-fluorouracil (5-FU), a common chemotherapeutic drug with the effect of miRNA expression up-regulation (*3*). The as-treated HeLa cells demonstrated enhanced Cy3 fluorescence after high-power 808-nm laser irradiation (fig. S26, second cycle, high), which was about 1.75-fold enhancement compared with that of untreated HeLa cells (Fig. 4G, NIR-DNA tweezer$_{Cy3/BHQ2}$, first cycle and second cycle, high). Subsequent low-power 808-nm irradiation quenched intracellular Cy3 fluorescence [Fig. 4G (NIR-DNA tweezer$_{Cy3/BHQ2}$, second cycle, low) and fig. S26 (second cycle, low)], suggesting the good reversibility of NIR-DNA tweezer$_{Cy3/BHQ2}$. In addition, CIB-3b, as a small-molecule inhibitor that effectively suppresses intracellular miRNAs expression by interfering with the signaling pathway between transactivation response RNA binding protein 2 (TRBP) and Dicer (*2*), was synthesized (fig. S27) and incubated with NIR-DNA tweezer$_{Cy3/BHQ2}$–treated HeLa cells. The as-treated HeLa cells demonstrated obviously suppressed Cy3 fluorescence after high-power 808-nm laser irradiation (fig. S28, second cycle, high), which was about 52.21% compared with that of untreated HeLa cells (Fig. 4H, NIR-DNA tweezer$_{Cy3/BHQ2}$, first cycle and second cycle, high). Subsequent low-power 808-nm laser irradiation also closed NIR-DNA tweezer$_{Cy3/BHQ2}$ and quenched intracellular Cy3 fluorescence [Fig. 4H (NIR-DNA tweezer$_{Cy3/BHQ2}$, second cycle, low) and fig. S28 (second cycle, low)]. Intracellular miRNA expression for 5-FU–treated HeLa cells and CIB-3b–treated HeLa cells was also quantified via quantitative reverse transcription PCR (qRT-PCR), respectively (fig. S29), which were about 1.86-fold and 60.39%, respectively, compared with that of untreated HeLa cells (fig. S30, qRT-PCR). The tendency of intracellular Cy3 fluorescence intensity for 5-FU–treated HeLa cells and CIB-3b–treated HeLa cells was similar to that of quantitative expression levels measured by PCR [fig. S30, confocal laser scanning microscope (CLSM) fluorescence]. HeLa cells was also incubated with the "irreversible" control o-NIR-DNA tweezer$_{Cy3/BHQ2}$ and treated with 5-FU and CIB-3b, respectively. O-NIR-DNA tweezer$_{Cy3/BHQ2}$ could effectively traced miR-21 expression up-regulation for 5-FU–treated HeLa cells and demonstrated enhanced intracellular Cy3 fluorescence after high-power 808-nm irradiation in second cycle [Fig. 4G (o-NIR-DNA tweezer$_{Cy3/BHQ2}$, second cycle, high) and fig. S31 (second cycle, high)]. However, it failed to trace miR-21 expression down-regulation for CIB-3b–treated HeLa cells and still showed high intracellular Cy3 fluorescence in second cycle alternate 808-nm irradiation [Fig. 4H (o-NIR-DNA tweezer$_{Cy3/BHQ2}$, second cycle) and fig. S32 (second cycle)], which indicated the generation of false-positive signal due to probe structure irreversibility.

NIR-DNA tweezer for in vivo continuous miRNA imaging

Subcutaneous HeLa tumor model was established on right forelimb of female BALB/c mice to evaluate the feasibility of NIR-DNA tweezer for in vivo miR-21 continuous imaging. UCNPs demonstrated NIR-II emission peak at 1060 nm under 808-nm irradiation corresponding to $^4F_{3/2} \rightarrow {}^4I_{11/2}$ transition of Nd^{3+}, and the conjugation of DNA strands for NIR-DNA tweezer$_{Cy5/BHQ3}$ did not affect NIR-II luminescence intensity of UCNPs (fig. S33); thus, its NIR-II emission was used to indicate the tumor accumulation of NIR-DNA tweezer$_{Cy5/BHQ3}$. NIR-DNA tweezer$_{Cy5/BHQ3}$ was intravenously injected into the tumor bearing mice and reached maximum in tumor grown position at 7 hours postinjection (fig. S34). To switch the reversible responses of NIR-DNA tweezer $_{Cy5/BHQ3}$ to miR-21, high power and low power of 808-nm laser irradiations were alternatively performed for 20 and 30 min, respectively, with 1-min "light-off" interval between every 10-min light exposure periods. During 10-min 808-nm laser irradiation period, the temperature of tumor tissue gradually increased from 33.5° to 37.5°C and rapidly decreased to 33.0°C during 1-min "light-off" interval (fig. S35, A and B). Considering that the normal physiological temperature of mice is 30° to 42°C (*39*), the light irradiation did not cause tissue damage (fig. S35C). To evaluate the in vivo stability of NIR-DNA tweezer$_{Cy5/BHQ3}$, we have measured the in vivo fluorescence ratio of Cy5/UCNP (FI_{Cy5}/FI_{UCNPs}) for NIR-DNA tweezer$_{Cy5/BHQ3}$–administrated mice corresponding to two complete cycles of alternating high- and low-power 808-nm NIR irradiations. During the entire experiment period, FI_{Cy5}/FI_{UCNPs} showed constant value of ~0.85 for high-power 808-nm NIR irradiation and another constant value of ~0.60 for low-power 808-nm NIR irradiation (fig. S36). This result confirmed both the in vivo structure and performance stability of NIR-DNA tweezer$_{Cy5/BHQ3}$.

For in vivo continuous miR-21 imaging, NIR-DNA tweezer$_{Cy5/BHQ3}$ was intravenously injected into the mice, which kept in closed status

during systematic circulation to avoid false-positive signal generation. Agomir (miR-21 mimic) and antiagomir (miR-21 inhibitor) were intratumorally injected for up-regulating and down-regulating tumor miR-21 expression. Agomir was intratumorally injected to up-regulate miR-21 expression at 7 hours after NIR-DNA tweezer$_{Cy5/BHQ3}$ administration, followed by high-density 808-nm irradiation and imaged at 2 hours later (Fig. 5A, first high power, imaging), which showed obvious FI_{Cy5}/FI_{UCNPs} ratiometric image at tumor site to indicate in vivo miR-21 expression (Fig. 5, B and C, group 1, first cycle, high). The tumor site was subsequently irradiated with low-power 808-nm radiation and imaged at 2 hours later (Fig. 5A, first low power, imaging), which showed largely suppressed in vivo FI_{Cy5}/FI_{UCNPs} ratiometric image, indicating NIR-DNA tweezer$_{Cy5/BHQ2}$ switching back to closed status with release of miR-21 (Fig. 5, B and C, group 1, first cycle, low). Antiagomir was then intratumorally injected to down-regulate miR-21 expression. The tumor site was irradiated with high-power 808-nm irradiation and imaged at 2 hours later (Fig. 5A, second high power, imaging), which demonstrated FI_{Cy5}/FI_{UCNPs} ratiometric recovery from tumor site with much lower intensity compared with that after agomir administration (Fig. 5, B and C, group 1, second cycle, high). Subsequent low-power 808-nm irradiation again suppressed FI_{Cy5}/FI_{UCNPs} ratiometric fluorescence at tumor site (Fig. 5, B and C, group 1, second cycle, low). These results indicated the capability of NIR-DNA tweezer for in vivo trace miRNA-21 expression fluctuations. Group 2 mice were set as the "constant power" control, which was administrated with NIR-DNA

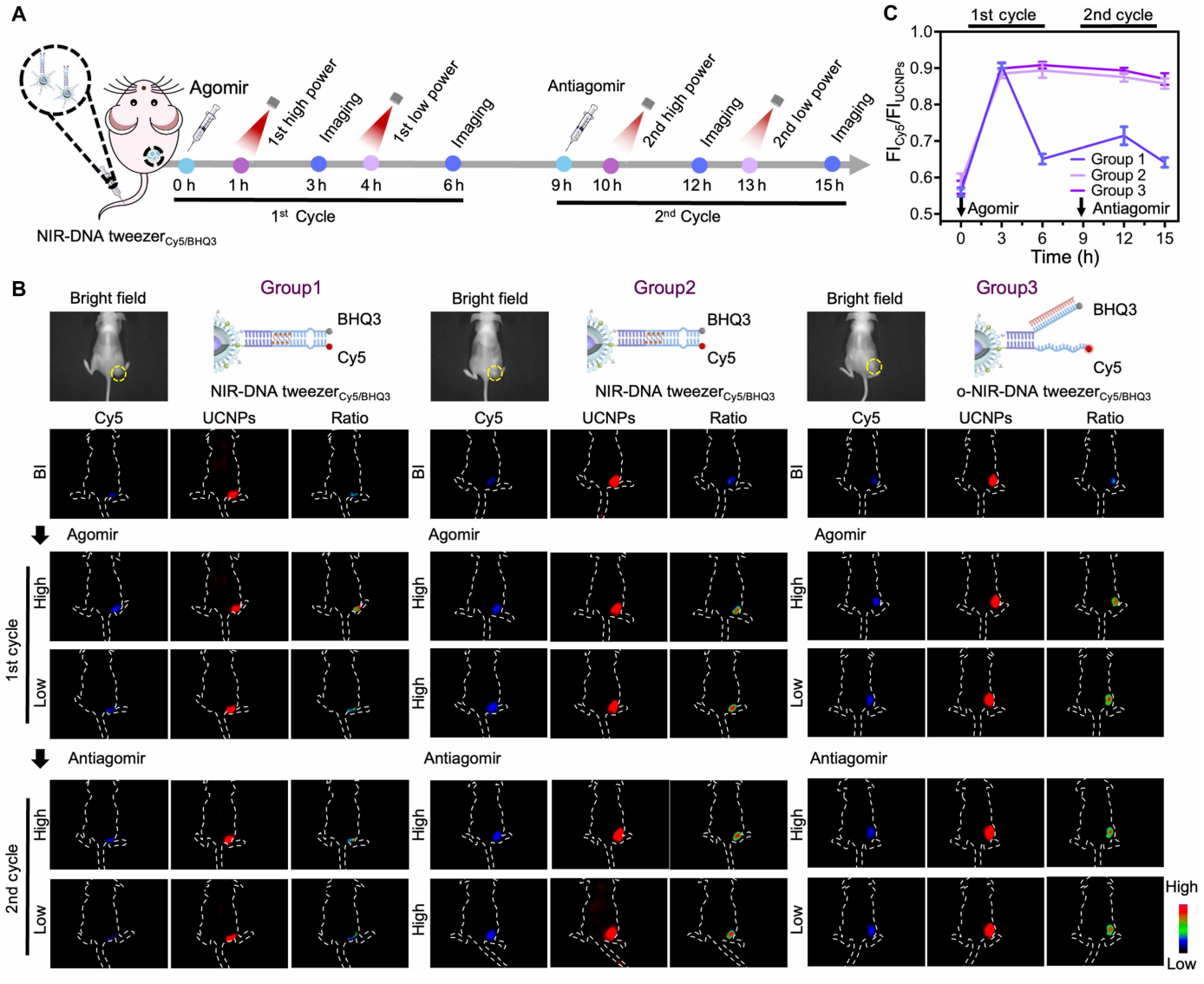

Fig. 5. NIR-DNA tweezer$_{Cy5/BHQ3}$ for in vivo dynamic miRNA imaging. (**A**) Schematic illustration of NIR-DNA tweezer$_{Cy5/BHQ3}$ administrated mice treated with agomir and antiagomir and two cycle of alternate high/low 808-nm irradiation. (**B**) In vivo Cy5, UCNPs, FI_{Cy5}/FI_{UCNPs} ratiometric image, and (**C**) corresponding ratiometric fluorescence intensity FI_{Cy5}/FI_{UCNPs} at tumor site for group 1 mice: administrated with NIR-DNA tweezer$_{Cy5/BHQ3}$ and exposed with two cycle of alternate high-/low-power 808-nm irradiation. Group 2 mice: administrated with NIR-DNA tweezer$_{Cy5/BHQ3}$ and exposed with two cycle of constant high-power 808-nm irradiation. Group 3 mice: administrated with o-NIR-DNA tweezer$_{Cy5/BHQ3}$ and exposed with two cycle of alternate high-/low-power 808-nm irradiation. All the mice groups were administrated with agomir and antiagomir at 0 and 9 hours, respectively. Error bars indicated means ± SD ($n = 5$).

tweezer$_{Cy5/BHQ2}$ and treated with agomir and antiagomir at same time spots as group 1 mice, which kept irradiated with high-power 808-nm laser irradiation each time. Therefore, group 2 mice remained high in vivo FI_{Cy5}/FI_{UCNPs} ratiometric fluorescence during the whole treatment process due to the lack of low-power 808-nm irradiation to renew NIR-DNA tweezer$_{Cy5/BHQ2}$ (Fig. 5, B and C, group 2). Group 3 mice were set as the "irreversible" control, which was administrated with o-NIR-DNA tweezer$_{Cy5/BHQ2}$ and treated with the same procedure as group 1 mice, which showed strong in vivo FI_{Cy5}/FI_{UCNPs} ratiometric fluorescence from tumor site during the whole experiment process due to the failure of status switch for o-NIR-DNA tweezer$_{Cy5/BHQ2}$ (Fig. 5, B and C, group 3). These results indicated the importance of NIR power density switching structure for continuous in vivo miRNA imaging. Major organs and tumors of mice were also collected for FI_{Cy5}/FI_{UCNPs} ratiometric fluorescence quantification, which was consistent with in vivo fluorescence imaging, and showed weak FI_{Cy5}/FI_{UCNPs} ratiometric fluorescence from tumor position for group 1 mice (fig. S37, group 1) and strong FI_{Cy5}/FI_{UCNPs} ratiometric fluorescence from tumor position for group 2 mice (fig. S37, group 2) and group 3 mice (fig. S37, group 3). Hematoxylin and eosin staining histopathology analysis of major organs (heart, liver, spleen, lung, and kidney) harvested from imaging mice exhibited little lesion compared with the untreated control group (fig. S38), demonstrating the good biocompatibility of imaging probe.

DISCUSSION

A NIR-DNA tweezer with photo-switchable binding affinities to miR-21 was presented here, which achieved in vivo tracing of miRNA expression fluctuations upon continuous chemotherapeutic drug and inhibitor treatments. Different from DNA probes for small molecules that have relatively lower binding affinities to recognition strand, designing reversible probes for miRNA with around 21 bp of recognition zone requires to modulate the binding affinities in a much wider range. Therefore, instead of modulating linker strand configuration that usually used for reversible small-molecule detections, here the hybridization zone of recognition/competitive strand for miR-21 was directly regulated upon alternate photo irradiations. UV irradiation induced transit status of DNA tweezer, partially exposed miR-21 recognition region, and endowed it high binding affinity to miR-21 with K_d value of ~21.74 nM, while Vis irradiation induced closed status of DNA tweezer and decreased miR-21 binding affinity to ~1880 nM. The photo-switched hybridization zones exhibited ~80-fold difference of miR-21 binding affinities, which was much larger compared with the binding affinities switching ranges of reported reversible detection probes (*24*).

To facilitate in vivo application, self-quenched NIR-DNA tweezer$_{Cy5/BHQ3}$ was obtained by conjugating DNA tweezer$_{Cy5/BHQ3}$ to UCNPs. The intensity ratio of UCNPs upconversion emission at Vis and UV regions (I_{Vis}/I_{UV}) was modulated through adjusting power of 808-nm excitation laser (*36*, *37*). Visible emission dominated the upconversion emission spectrum with I_{Vis}/I_{UV} of 3.06 at low excitation power of 808-nm light at 0.028 W, while UV emission was intense at high excitation power of 808 nm light, and I_{Vis}/I_{UV} saturated at 1.39 at 1.16 W. Considering that the molar attenuation coefficient of Azo trans-isomer (22,000 M^{-1} cm^{-1}) (*38*) is much larger than that of Azo *cis* isomer (400 M^{-1} cm^{-1}) (*38*), UV upconversion emission energy was used more efficiently compared with that of Vis upconversion emission at high excitation power, which facilitated trans-to-cis isomerization of Azo. On the other hand, the UV upconversion emission of UCNPs was too weak to make effect at low excitation power; thus, the dominant Vis upconversion emission took effort to drive the reverse cis-to-trans isomerization of Azo. NIR-DNA tweezer$_{Cy5/BHQ3}$ was intravenously administrated and originally stayed in closed status with self-quenched Cy5 fluorescence. By irradiating tumor grown position with high-power 808-nm light, NIR-DNA tweezer was switched to transit status to expose half of miR-21 recognition region, and subsequent miR-21 binding recovers Cy5 fluorescence. By irradiating tumor grown position with low-power 808-nm light, NIR-DNA tweezer$_{Cy5/BHQ3}$ was switched to closed status, which released miR-21 from DNA tweezer and erased Cy5 signal for reversible imaging. The as-presented NIR-DNA tweezer demonstrated accurate tracing of miR-21 expression fluctuations both at cellular level upon continuous chemotherapeutic drug 5-FU and inhibitor CIB-3b treatments and in vivo upon continuous agomir and antiagomir treatments. On the contrary, the nonreversible control DNA tweezer in lack of signal erasing capability showed false-positive signal both at cellular level and in vivo when miR-21 expression decreased. This work would have potential application for in vivo dynamic imaging of nucleic acid biomarkers and disease theranostics.

Although the stability of DNA duplexes may lead to relatively slow Azo isomerization rates (*24*), miRNA expression change upon drug or inhibitor treatments usually takes hours (*2*, *40*), which guarantees enough time for the binding affinities switching of NIR-DNA tweezer. Using of 808-nm irradiation light with low heating effect (*41*) as stimulus for driving binding affinities conversion and adding "light-off" intervals in irradiation periods also help to decrease body damage of photo-irradiation process. By conjugating ternary photoswitch DNA structures with rapidly switched structures to UCNPs could dynamically enhance tweezer statuses' switching efficiency and extend its application in tracing fast biological processes.

MATERIALS AND METHODS

Materials and reagents

Rare-earth (III) anhydrous chloride (Yb, Y, and Tm), sodium hydroxide (NaOH), ammoniumfluoride (NH_4F) were purchased from Aladin Ltd. (Shanghai, China). Ammonium persulfate (APS), acetone, cyclohexane, isopropyl alcohol, *N*,*N*,*N*′,*N*′-tetramethylethylenediamine (TEMED) were purchased from SCRC Ltd. (Shanghai, China). DSPE-PEG-FA [molecular weight (M_w) = 5000], DSPE-PEG-DBCO (M_w = 2000), DSPE-mPEG (M_w = 2000), and DSPE-PEG-NH_2 (M_w = 2000) were purchased from PengSheng Biotech (Shanghai, China). Oleic acid (OA), 1-octadecene (ODE), and acrylamide (40%) were purchased from Sigma-Aldrich Co. Ltd. (Shanghai, China). Dulbecco's modified Eagle's medium (DMEM), fetal bovine serum (FBS), and CCK-8 were bought from Keygen Biotech (Nanjing, China). LysoTracker Green, Lipofectamine 2000 reagent, and Opti-MEM were purchased from Thermo Fisher Scientific Inc. (Waltham, USA). RNAiso plus, Mir-X miRNA First-Strand Synthesis assay kit, and TB Green Premix Ex Taq II were purchased from Bohaode Biotech. Co. Ltd. (Nanjing, China). MiRNA inhibitor, miRNA mimics, agomir, antiagomir, and DEPC-teated water were purchased from GenePharma Co. Ltd. (Shanghai, China). The 10× tris-borate EDTA (TBE) premixed powder and all of the DNA oligonucleotides were synthesized and purified by Sangon Biotech Co. Ltd. (Shanghai, China) with sequences listed in table S2.

Apparatus

Gel electrophoresis was conducted on the PowerPac basic electrophoresis analyzer (Bio-Rad, USA). Fluorescence spectra were acquired on the FluoroMax-4 spectrofluorophotometer (Hitachi, Japan). Upconversion luminescence spectra were recorded on F-7000 spectrometer (Hitachi, Japan) under external 808-nm laser excitations. Absorption spectra were obtained with an UV-3600 UV-vis-NIR spectrophotometer (Shimadzu Company, Japan). Transmission electron microscopic images were carried out on JEM-2800 transmission electron microscope (JEOL Ltd., Japan). The cell images were carried out on TCS SP8 STED 3X CLSM (Leica, Germany). CCK-8 assays were performed on Hitachi/Roche System Cobas 6000 (Bio-Rad, USA). In vivo fluorescence imaging was carried out using NIROPTICS/ Monet IGS-1000 in vivo imaging system (Suzhou NIR-Optics Technology Co., Ltd., China).

MD simulations for DNA tweezer

The models for three status of DNA tweezer were constructed for MD simulations: (i) closed DNA tweezer with four "trans-" isomer Azo molecules inserted into the switch region of C-DNA between every two bases. Azo was linked to nucleic acid backbone via a D-threoninol linker. (ii) Transit DNA tweezer with four "cis-" isomer Azo inserted into the switch region of C-DNA between every two bases. (iii) Open DNA tweezer, a ternary model consisting of the DNA tweezer and miR-21, with Azo remaining in cis-isomer and miR-21 hybridized to the recognition region of R-DNA. The atomic coordinates of all models were generated using Discovery Studio and Materials Studio software packages.

The DNA complexes were solvated in a periodic rectangular water box, with a 12-Å water buffer maintained between any atom and the edge of the simulation box. The system was then neutralized by adding Cl^- and Na^+ ions to adjust the ionic concentration to 0.137 M. The CHARMM36 force field (*42*), along with the TIP3P_CHARMM water model (*43*), was applied to all systems. The CGenFF (*44*) server was used to generate parameters for the Azo residue. The Verlet algorithm (*45*) with a 1.2-nm cutoff was used for van der Waals interactions, while electrostatic interactions were calculated using the particle-mesh Ewald method with a 1.2-nm cutoff for short-range interactions. In the following steps 2 to 4, bonds involving hydrogen atoms were constrained using the linear constraint solver algorithm with a 2-fs time step. Periodic boundary conditions were applied throughout the simulations.

MD simulations were conducted using GROMACS 2022.2 (*46*), following the steps outlined below: (i) Energy minimization: The system underwent energy minimization using the steepest descent algorithm until the maximum force was reduced to below 10.0 kJ mol^{-1}. (ii) NVT equilibration: The system was equilibrated in the NVT ensemble at 310 K for 100 ps using the velocity rescaling (*47*) method for temperature control, with heavy atoms of the DNA restrained (1000 kJ mol^{-1} nm^{-2}). (iii) NPT equilibration: Following NVT equilibration, the system was equilibrated at 1 bar and 310 K for 100 ps in the NPT ensemble, with the same restraints. The temperature was controlled using the velocity rescaling (*47*) method, and the pressure was regulated with the Parrinello-Rahman (*48*) method. (iv) MD simulations were performed for 400 ns in the NPT ensemble (1 bar, 310 K), with coordinates and energies saved every 10.0 ps.

The interaction energies between C-DNA_{Azo} and R-DNA were calculated by defining energy groups and using the GROMACS rerun trajectory method. In line with the approach reported by Barbosa *et al.* (*49*), contributions from the DNA backbone atoms, including the negatively charged phosphate groups, were excluded in these calculations.

Binding affinity measurements of DNA tweezers

All binding affinity assays were performed in Hepes buffer (10 mM, pH 7.5) containing 15 mM NaCl, 1 mM $MgCl_2$, and 140 mM KCl. $DNA\ tweezers_{Alex/Cy3}$ was prepared by hybridizing 150 μl of 1 μM C-$DNA_{Azo/Cy3}$ with 150 μl of 1 μM R-DNA_{Alex} in phosphate-buffered saline (PBS) buffer at 37°C for 1 hour, forming a duplex structure. For transit state DNA tweezer binding affinities measurements, 150 μl of 0.5 μM $DNA\ tweezers_{Alex/Cy3}$ was irradiated with a 365-nm laser for 5 min, followed by incubation with miR-21 (final concentration of 0 to 1000 nM) in assay buffer at 37°C for 2 hours. Fluorescence emissions were recorded at 520 nm (Alexa Fluor 488) and 560 nm ($FRET_{Alexa\text{-}Cy3}$) under 480-nm excitation. Closed state DNA tweezer binding affinity measurement was assessed identically but with Vis irradiation.

FRET ratio calculation and binding affinity determination

FRET ratio was calculated according to previously reported approach (*24*). Alexa Fluor 488 emission (F_{Alex}) and Alexa-Cy3 FRET emission (F_{FRET}) were measured with 480-nm excitation and 520-nm and 560-nm emission, respectively, and F_{Alex} and F_{FRET} versus miR-21 concentration (c) data were processed by subtracting the background values obtained from buffer alone. Each value was obtained from triplicate measurements, and FRET ratio (R_{FRET}) for each replicate was calculated as

$$R_{FRET} = F_{FRET}/\left(F_{Alex} + F_{FRET}\right) \quad (1)$$

To calculate the binding affinity of DNA tweezers to the target miR-21 in closed and transit status, the above-obtained FRET ratios were fitted to a Langmuir isotherm

$$R_{FRET} = A^* c/\left(K_D + c\right) + y_0 \quad (2)$$

where K_D was the binding affinity, c is miR-21 concentration, y_0 is the background FRET ratio in the absence of miR-21, and A is the range of FRET ratio change.

Fluorescence kinetics measurements of light-triggered miR-21 binding to DNA tweezer

All kinetic measurements were conducted in Hepes buffer (10 mM, pH 7.5) containing 15 mM NaCl, 1 mM $MgCl_2$, and 140 mM KCl. $DNA\ tweezers_{Alex/BHQ1}$ was prepared by hybridizing 100 μl of 1 μM C-$DNA_{Azo/Alex}$ with 100 μl of 1 μM R-DNA_{BHQ1} in Hepes buffer at 37°C for 1 hour. For miR-21 binding analysis, 90 μl of 0.5 μM $DNA\ tweezers_{Alex/BHQ1}$ was photoactivated with UV irradiation (5 min), followed by addition of 10 μl of miR-21 (final concentration of 100 nM). For miR-21 release analysis, the above-mentioned open status $DNA\ tweezers_{Alex/BHQ1}$ was exposed to Vis irradiation (5 min) and UV irradiation (5 min), respectively. Alexa Fluor 488 fluorescence was recorded at 520 nm under 480-nm excitation with 1-min intervals.

Synthesis of UCNPs

Multishell structured lanthanide UCNPs was synthesized via one-pot successive layer-by-layer protocol. The upconversion core, $NaYF_4$:0.5% Tm, 30% Yb, was prepared by mixing 0.695 mmol of YCl_3, 0.3 mmol of $YbCl_3$ and 0.05 mmol of $TmCl_3$ in a three-necked flask containing 5 ml of OA and 15 ml of ODE. The mixture was heated to 150°C for

90 min under vacuum to obtain transparent solution and cooled down to 45°C. Subsequently, 10 ml of methanol solution containing 4 mmol of NH_4F and 2.5 mmol of NaOH was added dropwise into the mixture and kept for 30 min. After complete evaporation of methanol at 80°C for 30 min, the reaction mixture was heated to 300°C gradually and kept for 90 min under nitrogen atmosphere. After naturally cooled down to room temperature, the as-obtained upconversion core $NaYF_4$:Tm,Yb was precipitated with acetone, washed with ethanol, and redispersed in 10 ml of cyclohexane for future use.

Inner shell precursors ($NaYF_4$:10% Yb, 40% Nd) were synthesized by adding 0.5 mmol of YCl_3, 0.1 mmol of $YbCl_3$, and 0.4 mmol of $NdCl_3$ in a three-necked flask containing 5 ml of OA and 15 ml of ODE. The mixture was heated to 150°C for 90 min under vacuum to obtain transparent solution. After cooling down to 45°C, 10 ml of methanol containing 4 mmol of NH_4F and 2.5 mmol of NaOH were dropwise added in the above mixture and stirred at 45°C for 30 min. The reaction mixture was heated to 80°C for 30 min to completely remove methanol to obtain inner shell precursor $NaYF_4$:Yb,Nd. Outer shell precursors $NaYF_4$:40% Nd was also synthesized following the same procedure as described above.

To prepare $NaYF_4$:Tm,Yb@$NaYF_4$:Yb,Nd@$NaYF_4$:Nd, 10 ml of the above-obtained upconversion core $NaYF_4$:Tm,Yb was mixed with 5 ml of OA and 15 ml of ODE. The mixture was heated to 80°C for 30 min to remove cyclohexane completely and further heated to 300°C under nitrogen atmosphere. After being heated to 150°C, 4 ml of the above-obtained inner shell precursor $NaYF_4$:Yb,Nd was hot injected in and stirred at 300°C for 20 min, which was repeated for three times to obtain $NaYF_4$:Tm,Yb@$NaYF_4$:Yb,Nd. Outer shell precursor $NaYF_4$:Nd was also hot-injected in and stirred at 300°C following the same procedure as described above to obtain UCNPs $NaYF_4$:Tm,Yb@$NaYF_4$:Yb,Nd@$NaYF_4$:Nd, which was precipitated with acetone and washed with ethanol and redispersed in cyclohexane for future use.

Preparation of NIR power density–regulated DNA tweezer (NIR-DNA tweezer)

The above-obtained UCNPs were transferred to liquid phase via phospholipids wrapping based on hydrophilic-hydrophobic interactions. The UCNPs-DBCO/FA were prepared according to a previously reported approach (*50*) with mixture of DSPE-mPEG, DSPE-PEG-DBCO, and DSPE-PEG-FA (mass ratios = 8:1:1). UCNPs-DBCO/FA/NH_2 were also synthesized according to the same procedure with mixture of DSPE-mPEG, DSPE-PEG-DBCO, DSPE-PEG-FA, and DSPE-PEG-NH_2 (mass ratios = 7:1:1:1).

To prepare NIR-DNA tweezer, 0.2 mg of above-obtained UCNPs-DBCO/FA was reacted with 200 μl of 1 μM above-obtained N_3-DNA $tweezer_{FAM/BHQ1}$ overnight at room temperature. The as-obtained NIR-DNA $tweezer_{FAM/BHQ1}$ was centrifuged, washed, and redispersed in Hepes buffer for further use. The f-NIR-DNA tweezer and o-NIR-DNA tweezer were synthesized by conjugating N_3-f-DNA $tweezer_{FAM/BHQ1}$ and N_3-o-DNA $tweezer_{FAM/BHQ1}$ to UCNPs-DBCO/FA, respectively, following the aforementioned procedure.

PAGE analysis

A 10% polyacrylamide gel was prepared by mixing 2.75 ml of water, 1.20 ml of 5× TBE buffer, 2.00 ml of 30% acrylamide, 48.00 μl of APS, and 6.00 μl of TEMED in ice bath. A 5 μl of 1 μM DNA sample was mixed with 1 μl of 6× Orange DNA Loading Dye. The gel electrophoresis was run at 110 V for 60 min in 1× TBE buffer, then stained with SYBR Gold Nucleic Acid Gel Stain (Thermo Fisher Scientific, USA), and scanned with a Molecular Imager Gel Doc XR.

Fluorescence kinetic studies of NIR-DNA tweezer in vitro

All kinetic measurements were conducted in Hepes buffer (10 mM, pH 7.5) containing 15 mM NaCl, 1 mM $MgCl_2$, and 140 mM KCl. For miR-21 binding analysis, 90 μl of NIR-DNA $tweezer_{Alex/BHQ1}$ (1 mg/ml) was exposed to 808-nm laser irradiation for 20 min at a high power density (2 W/cm^2), followed by addition of 10 μl of miR-21 (final concentration of 10 nM). For miR-21 release analysis, 90 μl of open status NIR-DNA $tweezer_{Alex/BHQ1}$ (1 mg/ml) and 10 μl of miR-21 (final concentration of 10 nM) were exposed to 808-nm laser irradiation for 30 min at a low power density (0.75 W/cm^2). Alexa Fluor 488 fluorescence was recorded at 520 nm under 480-nm excitation with 1-min intervals.

In vitro reversible detection of miRNA-21

Configurations of DNA tweezer were switched by regulating Azo isomerization via alternate UV/Vis exposure. To switch DNA tweezer to open status with Azo in cis-configuration, 250 μl of 0.5 μM above-prepared N_3-DNA $tweezer_{FAM/BHQ1}$ was exposed to 365-nm laser irradiation for 5 min and simultaneously incubated with 10 nM miRNA-21 at 37°C for 30 min, and the corresponding FAM fluorescence recovery was measured under 480-nm excitation. To regulate DNA tweezer to closed status with Azo in trans-configuration, the above mixture was exposed to 456-nm laser irradiation for 5 min and simultaneously incubated at 37°C for another 30 min to observe FAM fluorescence change. This process was repeated for three cycles to verify the reversibility of DNA tweezer switching between open and closed status.

Configurations of NIR-DNA tweezer were switched by regulating Azo isomerization via alternate high and low power density of 808-nm NIR irradiation. To regulate DNA tweezer to open status with Azo in cis-configuration, 200 μl of NIR-DNA $tweezer_{FAM/BHQ1}$ (1 mg/ml) was exposed to 808-nm laser irradiation for 20 min at a high power density (2 W/cm^2) and simultaneously incubated with 10 nM miRNA-21 at 37°C for 30 min, and the corresponding FAM fluorescence recovery was measured under 480-nm excitation. To regulate DNA tweezer to closed status with Azo in trans-configuration, the above mixture was exposed to 808-nm laser irradiation for 30 min at a low power density (0.75 W/cm^2) and then incubated at 37°C to observe FAM fluorescence change. This process was repeated for three cycles to verify the reversibility of DNA tweezer switching between open and closed status. The f-NIR-DNA tweezer and the o-NIR-DNA tweezer served as control groups for the detection of miRNA-21, following the same procedure.

To verify the reaction sensitivity of NIR-DNA $tweezer_{FAM/BHQ1}$ to target miRNA, it was incubated with various concentrations (0 to 50 nM) of miRNA-21 after 20 min of high power density 808-nm NIR irradiations (2 W/cm^2), FAM fluorescence recovery was recorded under 480-nm excitation. To verify the reaction specificity of NIR-DNA $tweezer_{FAM/BHQ1}$ to target miRNA-21, it was incubated with 100 nM single base–mismatched miRNA-21 (M1), miRNA-155, miRNA-205, and miRNA-375 after 20 min of high power density 808-nm NIR irradiations (2 W/cm^2), and FAM fluorescence recovery was recorded under 480-nm excitation.

Cell culture

HeLa cells were cultured in DMEM media containing 10% FBS, penicillin (100 U/ml), and streptomycin (100 μg/ml) at 37°C in a

humidified atmosphere containing 5% CO_2 and 95% air. Cell numbers were determined with Countess II automated cell counter (Invitrogen, USA).

Cytotoxicity of NIR-DNA tweezer

CCK-8 assay was performed to evaluate cytotoxicity of NIR-DNA tweezer. HeLa cells suspension were seeded in a 96-well plate and incubated at 37°C overnight and subsequently incubated with various concentrations of NIR-DNA tweezer (0 to 200 μg/ml) for another 24 hours under the following conditions respectively: (i) without 808-nm light irradiation, (ii) with high power density 808-nm laser irradiation (2 W/cm^2), and (iii) with low power density 808-nm laser irradiation (0.75 W/cm^2). After that, CCK-8 solution (10 μl) was added to each well and incubated with the cells for 4 hours. Last, the absorbance of each well was measured at 450 nm by a Bio-Rad microplate reader.

Characterization of intracellular delivery of NIR-DNA tweezer

Lysosomal colocalization experiment was performed to verify the endocytosis of NIR-DNA tweezer. NIR-DNA tweezer$_{Red}$ (100 μg/ml) was incubated with HeLa cells for different periods of time and subsequently incubated with 50 nM LysoTracker Green PBS solution for 10 min, washed three times, and imaged with CLSM.

Probe integrity of NIR-DNA tweezers

Colocalization experiment of Texas Red and UCNPs upconversion emission was performed by incubating above-obtained NIR-DNA tweezer$_{Red}$ (100 μg/ml) with HeLa cells in DMEM for 24 hours and washed three times. Fluorescence images (Texas Red fluorescence was collected at 607 to 680 nm with 595-nm excitation, and UCNPs was collected at 430 to 500 nm with 808 nm excitation) of cells was captured by TCS SP5 CLSM.

Intracellular fluorescence kinetic studies of NIR-DNA tweezers

HeLa cells were seeded in four-well confocal dishes and incubated at 37°C for 24 hours and subsequently incubated with NIR-DNA tweezer$_{Cy3/BHQ2}$ (100 μg/ml). After rinsing the as-treated cells with PBS, it was exposed to high power density 808-nm laser irradiation for 20 min. Real-time Cy3 fluorescence images of cells were captured with CLSM. The as-treated cells were then subjected to low power density 808-nm laser irradiation for 30 min. Then, the real-time intracellular Cy3 fluorescence intensity was measured with CLSM.

Dynamic imaging of intracellular miRNA-21

A self-quenched NIR-DNA tweezer$_{Cy3/BHQ2}$, f-NIR-DNA tweezer$_{Cy3/BHQ2}$, and o-NIR-DNA tweezer$_{Cy3/BHQ2}$ were prepared to investigate dynamic changes of intracellular miRNA-21 expressions. HeLa cells were seeded in four-well confocal dishes and incubated at 37°C for 24 hours and subsequently incubated with above-obtained NIR-DNA tweezer$_{Cy3/BHQ2}$ (100 μg/ml), f-NIR-DNA tweezer$_{Cy3/BHQ2}$, and o-NIR-DNA tweezer$_{Cy3/BHQ2}$ for 11 hours. After rinsing the as-treated cells with PBS, it was exposed to high power density 808 nm laser irradiation for 20 min, and incubated at 37°C for 30 min. Intracellular Cy3 fluorescence recovery was measured with CLSM. The as-treated cells were then subjected to low power density 808-nm laser irradiation for 30 min and incubated at 37°C for 30 min. Intracellular Cy3 fluorescence intensity was measured with CLSM. This process was repeated for two cycles, and Cy3 fluorescence intensity change was recorded after each time light irradiation.

To mimic intracellular miRNA-21 expression fluctuations, miRNA-21 mimic and miRNA-21 inhibitor were transfected into HeLa cells. Cells were seeded in four-well confocal dishes and incubated at 37°C for 24 hours, the cells were randomly divided into three groups: In group 1, the HeLa cells were incubated with NIR-DNA tweezer$_{Cy3/BHQ2}$ (100 μg/ml) and successively transfected with 1 μM miRNA-21 mimic and 1 μM miRNA-21 inhibitor, with 6-hour gap between two transfections. In group 2, the HeLa cells were incubated with NIR-DNA tweezer$_{Cy3/BHQ2}$ (100 μg/ml) for 11 hours and then transfected with 1 μM miRNA-21 mimic for 6 hours. In group 3, the HeLa cells were incubated with o-NIR-DNA tweezer$_{Cy3/BHQ2}$ (100 μg/ml) for 11 hours and successively transfected with 1 μM miRNA-21 mimic and 1 μM miRNA-21 inhibitor, with 6-hour gap between two transfections. The as-treated cells were exposed to high power density 808-nm laser irradiation for 20 min and incubated at 37°C for 30 min. Intracellular Cy3 fluorescence recovery was measured with CLSM. The as-treated cells were then subjected to low power density 808-nm laser irradiation for 30 min and incubated at 37°C for another 30 min. Intracellular Cy3 fluorescence recovery was measured with CLSM.

To evaluate the capability of NIR-DNA tweezer for dynamic imaging of intracellular miRNA-21 expression fluctuation induced by chemotherapy drugs, HeLa cells was treated with 5-FU (a chemotherapy drug) and CIB-3b (a small-molecule inhibitor) for up-regulation and down-regulation of intracellular miRNA-21 expression, respectively. CIB-3b was synthesized according to a previously reported approach (*2*). ^{1}H nuclear magnetic resonance (NMR) (400 MHz, chloroform-d) δ = 8.01 (d, *J* = 8.9 Hz, 2H), 6.95 (d, *J* = 8.9 Hz, 2H), 4.42 (q, *J* = 7.1 Hz, 2H), 3.86 (s, 3H), 2.69 (s, 3H), 1.42 (t, *J* = 7.1 Hz, 3H); ^{13}C NMR (100 MHz, chloroform-d) δ = 162.6, 161.6, 159.8, 155.6, 128.6, 128.3, 119.4, 114.1, 61.0, 55.4, 14.4, 12.2. Cells were seeded in four-well confocal dishes and incubated at 37°C for 24 hours and subsequently incubated with NIR-DNA tweezer$_{Cy3/BHQ2}$ (100 μg/ml) for 11 hours. The as-treated cells were exposed to high power density 808-nm laser irradiation for 20 min, subsequently subjected to low power density 808-nm laser irradiation for 30 min, and incubated for 30 min after each time irradiations. The as-treated cells were randomly divided into two groups: Group 1 was transfected with 10 μM 5-FU for 6 hours, and group 2 was transfected with 100 μM CIB-3b for 6 hours. The as-treated cells were exposed to high power density 808-nm laser irradiation for 20 min, subsequently subjected to low power density 808-nm laser irradiation for 30 min, and incubated for 30 min after each time light irradiation. Intracellular Cy3 fluorescence was imaged with CLSM after each time light irradiation. The HeLa cells were incubated with o-NIR-DNA tweezer$_{Cy3/BHQ2}$ and served as control groups for intracellular miRNA-21 detection according to the same procedure.

qRT-PCR quantification of intracellular miRNA-21 expression

Intracellular miRNA-21 expressions levels in HeLa cells, miRNA-21 mimics, miRNA-21 inhibitor, 5-FU, and CIB-3b, respectively, pretreated HeLa cells were quantified using qRT-PCR. Total miRNAs were extracted from target cells by RNAiso Plus according to reagent protocol. cDNA was prepared by Mir-X miRNA First-Strand Synthesis assay kit. Standard curve was constructed with cycle threshold (Ct) values for various concentrations of miRNA-21, and the expression levels of cellular extracted miRNA-21 were calculated on the basis of standard curve.

In vivo miRNA-21 dynamic imaging

Female BALB/c nude mice with 5 to 6 weeks old were purchased from Jicui Yaokang Biomedical Biotech. Co., Ltd. (Nanjing, China). All animal experiments were performed in accordance with the National Institutes of Health (NIH) *Guidelines for the Care And Use of Laboratory Animals* (NIH publication no. 85-23 Rev. 1985) and approved by the Animal Ethical and Welfare Committee of Nanjing University with approval no. IACUC-2404009. HeLa subcutaneous tumor model was established by injecting 100-μl mixture of 1× PBS and matrix glue at a volume ratio of 1:1 containing 2×10^7/ml HeLa cells into the armpit of mice. In vivo tumor miRNA expression regulation and imaging were preformed after the tumor size reached 50 mm^3 (mice reached 2 to 3 weeks).

For in vivo stability assessment of the NIR-DNA tweezers, the as-obtained HeLa tumor bearing mice were first intravenously injected with 200 μl of NIR-DNA $tweezer_{Cy5/BHQ3}$ (1 mg/ml) and irradiated with high power density 808-nm laser (2 W/cm^2) for 20 min at 2, 10 hours, and low power density 808-nm laser (0.75 W/cm^2) at 6 and 14 hours. The Cy5 fluorescence and UCNP (1060 nm) fluorescence images were collected at 0, 4,8, 12, and 16 hours postinjection through the NIROPTICS/Monet IGS-1000 in vivo imaging system.

For in vivo miRNA imaging, the as-obtained HeLa tumor bearing mice were first intravenously injected with 200 μl of NIR-DNA $tweezer_{Cy5/BHQ3}$ (1 mg/ml) or o-NIR-DNA $tweezer_{Cy5/BHQ3}$. To demonstrate the feasibility of NIR-DNA $tweezer_{Cy5/BHQ3}$ in dynamic miRNA-21 in vivo imaging, agomir (miRNA-21 mimic) and antagomir (miRNA-21 inhibitor) were used to up-regulate and down-regulate tumor miRNA-21 expression concentrations, respectively. A 40 μl of agomir (0.5 mg/kg) was intratumorally injected at 7 hours after administration of NIR-DNA $tweezer_{Cy5/BHQ3}$, and 40 μl of antagomir (1.0 mg/kg) was intratumorally injected after 9 hours. The as-treated mice were divided into three groups: Group 1 mice was preadministrated with NIR-DNA $tweezer_{Cy5/BHQ3}$ and irradiated with high power density 808-nm laser (2 W/cm^2) for 20 min at 1 and 10 hours and low power density 808-nm laser (0.75 W/cm^2) at 4 and 13 hours after agomir administration, respectively; group 2 mice was preadministrated with NIR-DNA $tweezer_{Cy5/BHQ3}$ and irradiated with high power density 808-nm laser (2 W/cm^2) for 20 min at 1, 4, 10, and 13 hours; group 3 mice was preadministrated with o-NIR-DNA $tweezer_{Cy5/BHQ3}$ and irradiated with irradiated with high power density 808-nm laser (2 W/cm^2) for 20 min at 1 and 10 hours and low power density 808-nm laser (0.75 W/cm^2) at 4 and 13 hours after agomir administration, respectively. The Cy5 fluorescence and UCNP (1060 nm) fluorescence images were collected at 3, 6, 12, and 15 hours postinjection through the NIROPTICS/Monet IGS-1000 in vivo imaging system. The mice were euthanized after in vivo imaging, and their main organs, including heart, liver, spleen, lung, kidney, and tumor were collected for ex vivo fluorescence imaging.

Supplementary Materials

This PDF file includes:

Figs. S1 to S38
Tables S1 and S2

REFERENCES

1. H. Dong, J. Lei, L. Ding, Y. Wen, H. Ju, X. Zhang, MicroRNA: Function, detection, and bioanalysis. *Chem. Rev.* **113**, 6207–6233 (2013).
2. T. Peng, Y. He, T. Wang, J. Yu, X. Ma, Z. Zhou, Y. Sheng, L. Li, H. Peng, S. Li, J. Zou, Y. Yuan, Y. Zhao, H. Shi, F. Li, W. Liu, K. Hu, X. Lu, G. Zhang, F. Wang, Discovery of a novel small-molecule inhibitor disrupting TRBP–dicer interaction against hepatocellular carcinoma via the modulation of microRNA biogenesis. *J. Med. Chem.* **65**, 11010–11033 (2022).
3. L. Rossi, E. Bonmassar, I. Faraoni, Modification of miR gene expression pattern in human colon cancer cells following exposure to 5-fluorouracil in vitro. *Pharmacol. Res.* **56**, 248–253 (2007).
4. S. Uhlmann, E. Mracsko, E. Javidi, S. Lamble, A. Teixeira, A. Hotz-Wagenblatt, K.-H. Glatting, R. Veltkamp, Genome-wide analysis of the circulating miRNome after cerebral ischemia reveals a reperfusion-induced MicroRNA cluster. *Stroke* **48**, 762–769 (2017).
5. K. Jia, P. Shi, X. Han, T. Chen, H. Tang, J. Wang, Diagnostic value of miR-30d-5p and miR-125b-5p in acute myocardial infarction. *Mol. Med. Rep.* **14**, 184–194 (2016).
6. M. S. Kumar, J. Lu, K. L. Mercer, T. R. Golub, T. Jacks, Impaired microRNA processing enhances cellular transformation and tumorigenesis. *Nat. Genet.* **39**, 673–677 (2007).
7. B. M. Ryan, A. I. Robles, C. C. Harris, Genetic variation in microRNA networks: The implications for cancer research. *Nat. Rev. Cancer* **10**, 389–402 (2010).
8. J. Zhao, Z. Li, Y. Shao, W. Hu, L. Li, Spatially selective imaging of mitochondrial microRNAs via optically programmable strand displacement reactions. *Angew. Chem. Int. Ed.* **60**, 17937–17941 (2021).
9. Y. Wang, Q. Yang, Z. Gao, H. Dong, Recent advance of RNA aptamers and DNAzymes for microRNA detection. *Biosens. Bioelectron.* **212**, 1144 (2022).
10. C. Wang, Y. Xie, X. Song, Z. Chao, K. Wu, Y. Fang, H. Zhao, H. Ju, Y. Liu, A NIR programmable in vivo miRNA magnifier for NIR-II imaging of early stage cancer. *Angew. Chem. Int. Ed.* **62**, e202312665 (2023).
11. X. Chen, Q. You, Y. Guo, J. Zhang, Q. Hu, C. Huang, Z. Wu, J. Deng, J. Xu, P. Zhao, M. Hu, Mini crRNA-mediated CRISPR/Cas12a system enhanced imaging of multiple microRNAs in cells. *Chem. Biomed. Imaging* **3**, 369–378 (2025).
12. G. Deng, S. Zhang, X. Peng, G. Ma, L. Liu, Y. Tan, P. Gong, B. Z. Tang, L. Cai, P. Zhang, Methylene blue: An FDA-approved NIR-II fluorogenic probe with extremely low pH responsibility for hyperchlorhydria imaging. *Chem. Biomed. Imaging* **2**, 683–688 (2024).
13. M. R. Jones, N. C. Seeman, C. A. Mirkin, Programmable materials and the nature of the DNA bond. *Science* **347**, 1260901 (2015).
14. H.-R. Chen, M.-L. Su, Y.-M. Lei, Z.-X. Ye, Z.-P. Chen, P.-Y. Ma, R. Yuan, Y. Zhuo, C.-Y. Yang, W.-B. Liang, Insights of Life Molecules' dynamic distribution in live cells via sequence–structure bispecific fluorescent RNA. *J. Am. Chem. Soc.* **145**, 12812–12822 (2023).
15. X. Liu, C.-H. Lu, I. Willner, Switchable reconfiguration of nucleic acid nanostructures by stimuli-responsive DNA machines. *Acc. Chem. Res.* **47**, 1673–1680 (2014).
16. M. P. O'Hagan, Z. Duan, F. Huang, S. Laps, J. Dong, F. Xia, I. Willner, Photocleavable ortho-nitrobenzyl-protected DNA architectures and their applications. *Chem. Rev.* **123**, 6839–6887 (2023).
17. D. Bobrovnikov, M. A. Makurath, C. H. Wolfe, Y. R. Chemla, T. Ha, Helicase activity modulation with on-demand light-based conformational control. *J. Am. Chem. Soc.* **145**, 21253–21262 (2023).
18. Y. Zhao, S. Gao, D. Song, Z. Ye, R. Xu, Y. Luo, Q. Xu, Lipidoid artificial compartments for bidirectional regulation of enzyme activity through nanomechanical action. *J. Am. Chem. Soc.* **145**, 551–559 (2022).
19. Y. Zhao, Z. Ye, D. Song, D. Wich, S. Gao, J. Khirallah, Q. Xu, Nanomechanical action opens endo-lysosomal compartments. *Nat. Commun.* **14**, 6645 (2023).
20. X. Zhang, S. Dhir, L. Melidis, Y. Chen, Z. Yu, A. Simeone, J. Spiegel, S. Adhikari, S. Balasubramanian, Optical control of gene expression using a DNA G-quadruplex targeting reversible photoswitch. *Nat. Chem.* **17**, 875–882 (2025).
21. A. S. Lubbe, W. Szymanski, B. L. Feringa, Recent developments in reversible photoregulation of oligonucleotide structure and function. *Chem. Soc. Rev.* **46**, 1052–1079 (2017).
22. C. Wang, M. P. O'Hagan, Z. Li, J. Zhang, X. Ma, H. Tian, I. Willner, Photoresponsive DNA materials and their applications. *Chem. Soc. Rev.* **51**, 720–760 (2022).
23. Y. Zhang, Y. Zhang, G. Song, Y. He, X. Zhang, Y. Liu, H. Ju, A DNA–azobenzene nanopump fueled by upconversion luminescence for controllable intracellular drug release. *Angew. Chem. Int. Ed.* **58**, 18207–18211 (2019).
24. T. Trinh, I. A. P. Thompson, F. Clark, J. M. Remington, M. Eisenstein, J. Li, H. T. Soh, A photoresponsive intramolecular triplex motif that enables rapid and reversible control of aptamer binding activity. *ACS Nano* **16**, 14549–14557 (2022).
25. X. Zhang, C. Song, K. Yang, W. Hong, Y. Lu, P. Yu, L. Mao, Photoinduced regeneration of an aptamer-based electrochemical sensor for sensitively detecting adenosine triphosphate. *Anal. Chem.* **90**, 4968–4971 (2018).
26. L. Zhang, X. Zhang, P. Feng, Q. Han, W. Liu, Y. Lu, C. Song, F. Li, Photodriven regeneration of G-quadruplex aptasensor for sensitively detecting thrombin. *Anal.Chem.* **92**, 7419–7424 (2020).
27. I. A. P. Thompson, L. Zheng, M. Eisenstein, H. T. Soh, Rational design of aptamer switches with programmable pH response. *Nat. Commun.* **11**, 2946 (2020).
28. A. Porchetta, A. Idili, A. Vallee-Belisle, F. Ricci, General strategy to introduce pH-induced allostery in DNA-based receptors to achieve controlled release of ligands. *Nano Lett.* **15**, 4467–4471 (2015).

29. J. Zhao, H. Chu, Y. Zhao, Y. Lu, L. Li, A NIR light gated DNA nanodevice for spatiotemporally controlled imaging of microRNA in cells and animals. *J. Am. Chem. Soc.* **141**, 7056–7062 (2019).
30. G. A. Calin, C. M. Croce, MicroRNA signatures in human cancers. *Nat. Rev. Cancer* **6**, 857–866 (2006).
31. D. S. B. Hoon, A. E. Giuliano, M. Terpenning, T. Nguyen, C. Kuo, S. Asaga, Direct serum assay for MicroRNA-21 concentrations in early and advanced breast cancer. *Clin. Chem.* **57**, 84–91 (2011).
32. S. He, J. Song, J. Qu, Z. Cheng, Crucial breakthrough of second near-infrared biological window fluorophores: Design and synthesis toward multimodal imaging and theranostics. *Chem. Soc. Rev.* **47**, 4258–4278 (2018).
33. Y. Zhu, M. Fujiwara, Installing dynamic molecular photomechanics in mesopores: A multifunctional controlled-release nanosystem. *Angew. Chem. Int. Ed.* **119**, 2291–2294 (2007).
34. C. Yao, P. Wang, X. Li, X. Hu, J. Hou, L. Wang, F. Zhang, Near-infrared-triggered azobenzene-liposome/upconversion nanoparticle hybrid vesicles for remotely controlled drug delivery to overcome cancer multidrug resistance. *Adv. Mater.* **28**, 9341–9348 (2016).
35. Z. Wei, Z. Chao, X. Zhang, J. Yu, F. Xiao, X. Zhang, L. Tian, NIR-II luminescent and multi-responsive rare earth nanocrystals for improved chemodynamic therapy. *ACS Appl. Mater. Interfaces* **15**, 11575–11585 (2023).
36. L. Wang, H. Dong, Y. Li, C. Xue, L.-D. Sun, C.-H. Yan, Q. Li, Reversible near-infrared light directed reflection in a self-organized helical superstructure loaded with upconversion nanoparticles. *J. Am. Chem. Soc.* **136**, 4480–4483 (2014).
37. X. Jie, H. Yang, Y. Su, Z. Xia, W. Wei, Time-resolved monitoring of intracellular processes with a cyclical on–off photoswitchable nanoprobe. *ACS Sens.* **5**, 40–49 (2019).
38. F. A. Jerca, V. V. Jerca, R. Hoogenboom, Advances and opportunities in the exciting world of azobenzenes. *Nat. Rev. Chem.* **6**, 51–69 (2022).
39. K. C. Agno, K. Yang, S. H. Byun, S. Oh, S. Lee, H. Kim, K. Kim, S. Cho, W. I. Jeong, J. W. Jeong, A temperature-responsive intravenous needle that irreversibly softens on insertion. *Nat. Bio. Eng.* **8**, 963–976 (2024).
40. J. Li, A. Wang, X. Yang, K. Wang, J. Huang, Orderly assembled, self-powered FRET flares for MicroRNA imaging in live cells. *Anal. Chem.* **93**, 6270–6277 (2021).
41. C. Liu, B. Liu, J. Zhao, Z. Di, D. Chen, Z. Gu, L. Li, Y. Zhao, Nd^{3+}-sensitized upconversion metal-organic frameworks for mitochondria-targeted amplified photodynamic therapy. *Angew. Chem. Int. Ed.* **59**, 2634–2638 (2020).
42. W. L. Jorgensen, J. Chandrasekhar, J. D. Madura, R. W. Impey, M. L. Klein, Comparison of simple potential functions for simulating liquid water. *J. Chem. Phys.* **79**, 926–935 (1983).
43. K. Vanommeslaeghe, E. Hatcher, C. Acharya, S. Kundu, S. Zhong, J. Shim, E. Darian, O. Guvench, P. Lopes, I. Vorobyov, A. D. Mackerell, CHARMM general force field: A force field for drug-like molecules compatible with the CHARMM all-atom additive biological force fields. *J. Comput. Chem.* **31**, 671–690 (2009).
44. L. Verlet, Computer "experiments" on classical Fluids. I. Thermodynamical properties of lennard-jones molecules. *Phys. Rev.* **159**, 98–103 (1967).
45. T. Darden, D. York, L. Pedersen, Particle mesh Ewald: An N·log(N) method for Ewald sums in large systems. *J. Chem. Phys.* **98**, 10089–10092 (1993).
46. M. J. Abraham, T. Murtola, R. Schulz, S. Páll, J. C. Smith, B. Hess, E. Lindahl, GROMACS: High performance molecular simulations through multi-level parallelism from laptops to supercomputers. *SoftwareX* **1-2**, 19–25 (2015).
47. G. Bussi, D. Donadio, M. Parrinello, Canonical sampling through velocity rescaling. *J. Chem. Phys.* **126**, 014101 (2007).
48. M. Parrinello, A. Rahman, Polymorphic transitions in single crystals: A new molecular dynamics method. *J. Appl. Phys.* **52**, 7182–7190 (1981).
49. N. Barbosa, L. Sagresti, G. Brancato, Photoinduced azobenzene-modified DNA dehybridization: Insights into local and cooperativity effects from a molecular dynamics study. *Phys. Chem. Chem. Phys.* **23**, 25170–25179 (2021).
50. S. Wang, L. Liu, Y. Fan, A. M. El-Toni, M. S. Alhoshan, D. Li, F. Zhang, In vivo high-resolution ratiometric fluorescence imaging of inflammation using NIR-II nanoprobes with 1550 nm emission. *Nano Lett.* **19**, 2418–2427 (2019).

Acknowledgments

Funding: The work was supported by the National Natural Science Foundation of China (22374073), the State Key Laboratory of Analytical Chemistry for Life Science (5431ZZXM2504), and the Program A for Outstanding PhD Candidates of Nanjing University. **Author contributions:** C.W. designed and performed all experiments, collected the experimental data, and made data analysis. Y.C. supplements all experiments mentioned in the review comments and conducts the associated data collection and analysis. L.Y. conducts theoretical calculations and corresponding data analysis. L.L. synthesized CIB-3b small molecule and conducted spectral analysis. Y.X. participates in DNA sequence design. X.D. participates in data collection and instrument maintenance in supplementing corresponding experiments. C.W. and L.Y. wrote the original draft. H.J. and provided advice and suggestions for the experiment data. G.Z. guides the theoretical calculation and revised the manuscript. Y.L. supervised the project and revised the manuscript. All the authors discussed the results. **Competing interests:** The authors declare that they have no competing interests. **Data and materials availability:** All data and code needed to evaluate and reproduce the results in the paper are present in the paper and/or the Supplementary Materials.

Submitted 28 May 2025
Accepted 9 December 2025
Published 9 January 2026
10.1126/sciadv.adz3560